

**An efficient algorithm for the inverse
problem in elasticity imaging by means of
variational r-adaption**

A. Arnold, O. T. Bruhns and J. Mosler

This is a preprint of an article accepted by:

Physics in Medicine and Biology (2011)

An efficient algorithm for the inverse problem in elasticity imaging by means of variational r -adaption

A. Arnold and O.T. Bruhns

Institute of Mechanics
Ruhr University Bochum
Ruhr University Bochum
D-44780 Bochum, Germany
E-Mail: bruhns@tm.bi.rub.de

J. Mosler

Materials Mechanics
Institute of Materials Research
Helmholtz-Zentrum Geesthacht
D-21502 Geesthacht, Germany
E-Mail: joern.mosler@hzg.de

SUMMARY

A novel finite element formulation suitable for computing efficiently the stiffness distribution in soft biological tissue is presented in this paper. For that purpose, the inverse problem of finite strain hyperelasticity is considered and solved iteratively. In line with (Arnold et al. 2010 Phys. Med. Biol. **55** 2035), the computing time is effectively reduced by using adaptive finite element methods. In sharp contrast to previous approaches, the novel mesh adaption relies on an r -adaption (re-allocation of the nodes within the finite element triangulation). This method allows to detect material interfaces between healthy and diseased tissue in a very effective manner. The evolution of the nodal positions is canonically driven by the same minimization principle characterizing the inverse problem of hyperelasticity. Consequently, the proposed mesh adaption is variationally consistent. Furthermore, it guarantees that the quality of the numerical solution is improved. Since the proposed r -adaption requires only a relatively coarse triangulation for detecting material interfaces, the underlying finite element spaces are usually not rich enough for predicting the deformation field sufficiently accurately (the forward problem). For this reason, the novel variational r -refinement is combined with the variational h -adaption (Arnold et al. 2010 Phys. Med. Biol. **55** 2035) to obtain a variational hr -refinement algorithm. The resulting approach captures material interfaces well (by using r -adaption) and predicts a deformation field in good agreement with that observed experimentally (by using h -adaption).

1 Introduction

Elasticity imaging also known as elastography is a non-invasive medical imaging technology allowing to visualize the stiffness distribution in biological tissue. It represents an effective method for detecting pathologies, e.g., breast cancer or prostate tumors, since diseased tissue is often stiffer than the surrounding material. This method dating back, at least, to [31], is still an active and ongoing area of biomechanical research, cf. [7, 14, 17, 18, 29, 33].

The underlying idea of elasticity imaging is the computation of the stiffness distribution in biological tissue by comparing experimentally measured data to their numerically predicted counterparts. More precisely, the displacement field characterizing the investigated biological tissue is determined first by using ultrasound or MRI signals, together with filtering techniques, see [30, 32]. Subsequently, this displacement field serves as input for computing the stiffness contribution. For that purpose, different methods can be

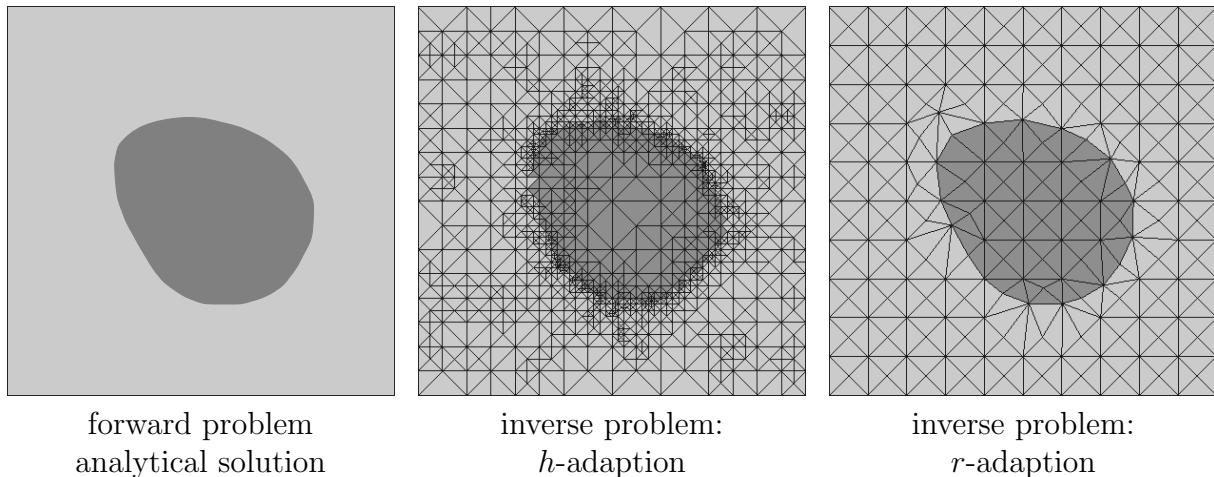


Figure 1: Biological tissue with one hard lump: Comparison of two different adaptive finite element methods applied to the inverse problem in elasticity (in h -adaption, the size of the finite elements is reduced, while the nodes are re-allocated in case of r -adaption). Both methods detect the material interface. However, the r -adaptive scheme requires significantly less finite elements.

applied, cf. [7, 17, 29, 41, 42]. All of them are based on certain constitutive assumptions. Since a material model taking also large strain effects into account is considered in the present paper, only iterative methods can be employed. Conceptually, the error between the measured displacement field and that predicted by a nonlinear forward problem depending on the unknown stiffness distribution is minimized within such methods. The high nonlinearity of the function to be minimized, the existence of several minima and the data noise associated with the measured displacements require special attention, cf. [7, 15, 17, 28, 29].

For computing the forward problem within the aforementioned iterative methods, the finite element method is usually employed. Accordingly, the numerical costs necessary for one iteration step as well as the quality of the solution depend crucially on the underlying spatial discretization. An effective way for reducing the computing time, while maintaining or improving the quality of the numerical solution is provided by adaptive finite element meshes, cf. [1, 45]. A first prototype of such strategies suitable for the inverse problem of hyperelasticity was recently proposed in [2]. It is based on the variational adaptive finite element methods as advocated in [24, 26, 27]. The underlying idea of this method is a local h -refinement governed by a variationally consistent error indicator. More precisely, only those elements are refined within this approach which lead to a significant decrease in the function to be minimized. The finite element meshes as well as the stiffness distribution resulting from the adaptive method [2] are sketched in figure 1. As can be seen, the material interfaces are captured by the mesh adaption, i.e., the elements' diameters are very small at material interfaces, while they are comparably coarse in the remaining domain. However, the number of elements necessary for detecting such interfaces is very large. For reducing this number and thus, for increasing the numerical efficiency further, a novel variationally consistent r -adaptive scheme is elaborated within the present paper. Conceptually, the nodal coordinates defining the finite element triangulation are optimized, cf. figure 1. Such a method has already been successfully applied to the forward problem discretized by standard displacement-driven finite elements, cf. [3, 21, 25, 43] (see also [11, 23]). It is closely related to classical Eshelby mechanics in

which the deformation of material defects such as internal interfaces is studied, see [9, 10]. In the present paper, the method originally advocated in [3, 21, 25, 43] is extended in two directions. First, since quasi-incompressible biological tissue is considered, the r -adaption is combined with a mixed finite element formulation. Secondly and equally importantly, it is elaborated for the inverse problem.

Since the proposed r -adaption requires only a relatively coarse triangulation for detecting material interfaces, the underlying finite element spaces are usually not rich enough for predicting the deformation field sufficiently accurately (the forward problem). For this reason, the novel variational r -refinement is combined with the variational h -adaption [2] to obtain a variational hr -refinement algorithm. The resulting approach captures material interfaces well (by using r -adaption) and predicts a deformation field in good agreement with that observed experimentally (by using h -adaption).

The structure of the paper is as follows: In section 2, the forward problem of hyperelasticity, together with a constitutive model suitable for the analysis of biological tissue, are briefly presented. The inverse problem of elasticity imaging and its numerical implementation are addressed in section 3. Two effective adaptive finite element methods are elaborated in sections 4 and 5. While section 4 is concerned with the variationally consistent h -adaption as published in [2], the novel r -adaptive strategy is elaborated in section 5. Finally, the aforementioned combined hr -refinement algorithm is described in 6.

2 The forward problem of hyperelasticity

Before explaining the inverse problem of hyperelasticity, it is essential to introduce and understand its underlying classical forward problem. Within this forward problem, the boundary conditions (prescribed displacements or stresses) as well as the material's response are assumed to be known, while the resulting deformation of the considered mechanical system is unknown and thus, it is to be computed. First, the fundamentals of the forward problem are briefly summarized in subsection 2.1. Subsequently, a standard numerical implementation by means of a mixed finite element formulation is shown in subsection 2.2. Further details on the nowadays well known forward problem can be found elsewhere, e.g., in [22, 44, 46].

2.1 Fundamentals

In the present subsection, some fundamentals of continuum mechanics are briefly introduced. Throughout the paper, a geometrically exact description is considered (large strains and deformations). This is necessary, since the strains within the experiments and those within the respective simulations are greater than 10%.

Following the most frequently used notations in continuum mechanics, the deformation of a hyperelastic solid \mathcal{B} occupying the domain \mathcal{B}_0 in its reference undeformed configuration is described by the nonlinear deformation mapping $\varphi(\mathbf{X})$. This function maps the position of a material point in the reference configuration $\mathbf{X} \in \mathcal{B}_0$ to its position in the current deformed configuration $\mathbf{x} \in \mathcal{B}_t$. Alternatively and as usually done within a geometrically linearized setting, the motion of a body can be characterized by the displacement field $\mathbf{u} = \varphi(\mathbf{X}) - \mathbf{X}$.

Clearly, both field variables φ and \mathbf{u} are not convenient for constitutive modeling. For that purpose, local measures of the (relative) deformation are more suitable. One such

measure is given by the deformation gradient $\mathbf{F} = \text{GRAD}\boldsymbol{\varphi} := \partial\mathbf{x}/\partial\mathbf{X}$ which is the basis for all strain tensors. Without loss of generality, the right Cauchy-Green tensor $\mathbf{C} = \mathbf{F}^T \cdot \mathbf{F}$ is chosen in the present paper.

Having defined the strain measure \mathbf{C} , the first Piola-Kirchhoff stress tensor \mathbf{P} can be computed. Since the mechanical response of biological tissue is to be approximated, a hyperelastic material model is adopted. Accordingly, by introducing the Helmholtz stored energy $W = W(\mathbf{F})$, standard thermodynamical arguments lead to

$$\mathbf{P} = \frac{\partial W(\mathbf{F})}{\partial \mathbf{F}}. \quad (1)$$

Clearly, in addition to the constraints imposed by the considered biological tissue, the stored energy functional has also to fulfill the principles of continuum mechanics such as the principle of objectivity $W = W(\mathbf{F}) = \hat{W}(\hat{\mathbf{C}})$ and certain growth conditions.

Biological tissue often shows a completely different mechanical response for volumetric and isochoric deformations. This can be taken into account by applying a decomposition of the Helmholtz energy of type

$$W(\mathbf{F}) = W(\hat{\mathbf{C}}, J) = W(\hat{\mathbf{C}}) + U(J), \quad (2)$$

cf. [13]. In (2), $W(\hat{\mathbf{C}})$ denotes the part of the Helmholtz energy associated with isochoric deformation, $U(J)$ is its volumetric counterpart, $J := \det \mathbf{F}$ represents the Jacobian determinant and $\hat{\mathbf{C}}$ is the isochoric right Cauchy-Green strain tensor, i.e.,

$$\hat{\mathbf{C}} := \hat{\mathbf{F}}^T \cdot \hat{\mathbf{F}}, \quad \text{with } \hat{\mathbf{F}} := J^{-1/3} \mathbf{F} \quad \Rightarrow \quad \det \hat{\mathbf{F}} = 1. \quad (3)$$

In the present paper, the stored energies corresponding to deviatoric and volumetric deformations are chosen as

$$W(\hat{\mathbf{C}}) := \frac{1}{2}\mu \left(\text{tr}(\hat{\mathbf{C}}) - 3 \right) \quad \text{and} \quad U(J) := \frac{K}{4} (J^2 - 1) - \frac{K}{2} \ln J. \quad (4)$$

As a result, the first Piola-Kirchhoff stress tensor reads

$$\mathbf{P} = \mathbf{P}_{\text{iso}} + \mathbf{P}_{\text{vol}} \quad (5)$$

with

$$\mathbf{P}_{\text{iso}} = \frac{\partial W(\hat{\mathbf{C}})}{\partial \mathbf{F}} = \mu J^{-\frac{2}{3}} \left(\mathbf{F} - \frac{1}{3} \text{tr}(\mathbf{C}) \mathbf{F}^{-T} \right) \quad \text{and} \quad (6)$$

$$\mathbf{P}_{\text{vol}} = \frac{\partial U}{\partial \mathbf{F}} = p J \mathbf{F}^{-T}, \quad \text{with } p := \frac{\partial U}{\partial J}. \quad (7)$$

As evident from (4), the material model is defined by means of two material parameters: the shear modulus μ and the bulk modulus K .

Assuming quasi-static conservative loadings, the resulting mechanical system (the boundary value problem) is characterized by a potential structure similar to that of the local constitutive model. More precisely, denoting the stored elastic energy of the total body as

$$\Pi_{\text{int}} = \int_{\mathcal{B}_0} W(\mathbf{F}) \, dV \quad (8)$$

and the energy associated with externally applied forces as $\Pi_{\text{ext}}(\boldsymbol{\varphi})$, the unknown deformation $\boldsymbol{\varphi}$ follows naturally from minimizing the total potential energy $\Pi = \Pi_{\text{int}} + \Pi_{\text{ext}}$ of the mechanical system, cf. [38]. Clearly, this minimization problem is constrained by prescribed deformations $\bar{\boldsymbol{\varphi}}$ at the Dirichlet boundary $\partial\mathcal{B}_{0u}$. Consequently, the resulting canonical optimization problem is given by

$$\inf_{\boldsymbol{\varphi} \in \mathcal{U}} \Pi, \quad \text{with } \mathcal{U} = \{\boldsymbol{\varphi} : \mathcal{B}_0 \rightarrow \mathcal{B}_t \mid \boldsymbol{\varphi} = \bar{\boldsymbol{\varphi}}, \forall \mathbf{X} \in \partial\mathcal{B}_{0u}\}. \quad (9)$$

Unfortunately, the physically and mathematically canonical and thus, very appealing optimization principle (9) cannot be used within the present paper. Since soft tissue shows an almost incompressible behavior, a straightforward discretization of $\inf \Pi(\boldsymbol{\varphi})$ by using classical deformation-driven finite elements would lead to pathological numerical locking effects, cf. [48]. For this reason and in line with [39, 40], a mixed finite element formulation based on a Hu-Washizu principle is applied. Within this mixed formulation, the deformation $\boldsymbol{\varphi}$, the pressure p and the volumetric strain Θ are introduced as independent variables. Following [46], the potential energy Π^{HW} reads

$$\Pi^{\text{HW}}(\boldsymbol{\varphi}, p, \Theta) = \int_{\mathcal{B}_0} (W(\hat{\mathbf{C}}) + U(\Theta) + p(J - \Theta)) \, dV + \Pi_{\text{ext}}(\boldsymbol{\varphi}). \quad (10)$$

In contrast to the principle of minimum potential energy (9), the Hu-Washizu principle represents a stationarity problem (saddle point). The necessary conditions for its extrema are given by (cf. [38])

$$D_{\Theta} \Pi^{\text{HW}} \gamma = \int_{\mathcal{B}_0} \gamma \left(\frac{\partial U(\Theta)}{\partial \Theta} - p \right) \, dV = 0, \quad (11)$$

$$D_p \Pi^{\text{HW}} q = \int_{\mathcal{B}_0} q (J - \Theta) \, dV = 0 \quad \text{and} \quad (12)$$

$$D_{\boldsymbol{\varphi}} \Pi^{\text{HW}} \cdot \boldsymbol{\eta} = \int_{\mathcal{B}_0} \text{Grad } \boldsymbol{\eta} : (\mathbf{P}_{\text{iso}} + \mathbf{P}_{\text{vol}}) \, dV = 0. \quad (13)$$

For the sake of clarity, externally applied forces have been neglected here. In (11)–(13), $D_{(\bullet)} \Pi^{\text{HW}}$ denotes the partial derivative of Π^{HW} with respect to (\bullet) and γ , q and $\boldsymbol{\eta}$ are the variations of the volumetric strain Θ , the pressure p and the deformation $\boldsymbol{\varphi}$, respectively.

2.2 Numerical implementation

A mixed finite element formulation based on the stationarity conditions (11)–(13) is briefly sketched here. This section serves mostly for introducing the notations used within the numerical implementations. Further details can be found, e.g., in [16, 48].

For discretizing the weak forms (11)–(13), a Bubnov-Galerkin discretization of the type

$$\mathbf{x}_e^h = \sum_{I=1}^{n_1} N_I^{\boldsymbol{\varphi}}(\boldsymbol{\xi}) \mathbf{x}^I \in \mathbb{P}_2 \quad \boldsymbol{\eta}_e^h = \sum_{I=1}^{n_1} N_I^{\boldsymbol{\varphi}}(\boldsymbol{\xi}) \boldsymbol{\eta}^I \in \mathbb{P}_2 \quad (14)$$

$$\Theta_e^h = \sum_{I=1}^{n_2} N_I^{\Theta}(\boldsymbol{\xi}) \Theta^I \in \mathbb{P}_0 \quad \gamma_e^h = \sum_{I=1}^{n_2} N_I^{\Theta}(\boldsymbol{\xi}) \gamma^I \in \mathbb{P}_0 \quad (15)$$

$$p^h = \sum_{I=1}^{n_3} N_I^p(\boldsymbol{\xi}) p^I \in \mathbb{P}_0 \quad q_e^h = \sum_{I=1}^{n_3} N_I^p(\boldsymbol{\xi}) q^I \in \mathbb{P}_0 \quad (16)$$

is employed. Here, the superscript I highlights variables associated with node I , N are shape functions and \mathbb{P}_i is the space containing all polynomials of order i . Following an isoparametric concept, the undeformed configuration is approximated in the same manner as its deformed counterpart, i.e.,

$$\mathbf{X}_e^h = \sum_{I=1}^{n_1} N_I^\varphi(\boldsymbol{\xi}) \mathbf{X}^I \in \mathbb{P}_2. \quad (17)$$

Based on the weak forms (11)–(13), together with the interpolations (14)–(17), the unknown deformation $\boldsymbol{\varphi}$ is computed from the discretized principle of virtual work (13). Inserting (14) into (13), this principle is approximated by

$$\boldsymbol{\eta}^I \cdot \mathbf{r}_e^I = 0 \quad \text{with} \quad \mathbf{r}_e^I := \int_{\mathcal{B}_0^e} (\mathbf{P}_{\text{iso}} + \mathbf{P}_{\text{vol}}) \cdot \frac{\partial N_I^\varphi}{\partial \mathbf{X}_e^h} dV_e. \quad (18)$$

Evidently, (18) is associated with the contribution of node I to the residual force acting at element e . The global counterpart $[\mathbf{r}] = \mathbf{0}$ is obtained by applying a classical assembling procedure. The resulting set of nonlinear equations is solved by means of a Newton scheme. This scheme requires the linearization of (18). Although this linearization is quite lengthy, since \mathbf{P} depends on \mathbf{x} , Θ as well as p , it can be computed in a straightforward manner. For that purpose, (11) and (12) have to be linearized first yielding the sensitivities of Θ and p with respect to the deformation field \mathbf{x} . Inserting these sensitivities into the linearization of (13) leads finally to a reduced stiffness relation of the type $[\mathbf{K}^{\Delta\mathbf{x}}][\Delta\mathbf{x}] = [\mathbf{r}]$. It is solved for $[\Delta\mathbf{x}]$ by means of the powerful solver PARDISO 3.2, cf. [36, 37]. Here, $[\mathbf{K}^{\Delta\mathbf{x}}]$ denotes the global stiffness matrix, $[\mathbf{r}]$ the global vector of internal forces and $[\mathbf{x}]$ the global vector of all nodal deformations. A detailed derivation of the element stiffness matrices can be found, e.g., in [2].

3 The inverse problem of hyperelasticity

While the boundary conditions and the material response are assumed as known for the forward problem and the deformation mapping is the unknown to be computed, the opposite holds for the inverse problem. More precisely, the boundary conditions, together with the deformation mapping are known and the material response represents the unknown. Clearly, such a problem is mathematically ill-posed. For this reason, the space of admissible material responses is usually decreased by considering a suitable family of constitutive laws. Within the present paper, this family is chosen as that spanned by the hyperelastic model based on the volumetric-deviatoric decomposition (see subsection 2.1; (1)–(4)). Consequently, the only unknowns are the shear modulus μ as well as the bulk modulus K . Fortunately, since fluid-saturated biological tissues are quasi-incompressible, K can be a priori chosen as sufficiently larger than μ and it can thus be fixed. As a result, the only remaining unknown variable characterizing the inverse problem of hyperelasticity is the spatial distribution of the shear modulus. The fundamentals of the inverse problem are discussed in subsection 3.1, while a numerical implementation is briefly sketched in subsection 3.2.

3.1 Fundamentals

In line with [28, 29, 33], the inverse problem of hyperelasticity can be stated as an optimization problem. For that purpose, the objective function

$$\mathfrak{g}(\mu) = \frac{1}{2} \|\mathcal{P}(\varphi(\mu) - \varphi^g)\|^2 + \frac{\alpha}{2} \|\mu - \mu^*\|^2 \quad (19)$$

is introduced. In (19), $\varphi = \varphi(\mu)$ denotes the deformation as predicted by the previously discussed mixed finite element formulation, φ^g is the measured deformation, \mathcal{P} is a projection operator taking into account that only the vertical component of the displacement field can be measured accurately ($\mathcal{P}(\varphi) = \varphi_2$), α is a regularization parameter and μ^* is a reference shear modulus. Accordingly, the first term in (19) defines the error between the measured and the computed deformation as a function in μ . Consequently, minimizing this term with respect to μ will lead to a shear modulus distribution complying well with the observed deformation. The second term in (19) is a so-called *Tikhonov*-type regularization, cf. [8]. It is required, since the inverse problem is usually highly ill-conditioned and several minima exist. Having defined the objective function (the error), the inverse problem of hyperelasticity is defined by the minimization problem

$$\inf_{\mu} \mathfrak{g}(\mu). \quad (20)$$

It is solved by utilizing the L-BFGS-B algorithm, see [4, 47].

3.2 Numerical implementation

For computing an approximation solution of problem (20), the finite element method is employed. For that purpose and in line with [16, 48], the functional $\mathfrak{g}(\mu)$ is decomposed into its element contributions, i.e.,

$$\mathfrak{g}(\mu) \approx \mathfrak{g}^h(\mu^h) = \sum_{e=1}^n \mathfrak{g}_e^h(\mu_e^h), \quad (21)$$

with n being the number of elements within the considered triangulation. According to (19), each element contribution is defined by

$$\mathfrak{g}_e^h(\mu_e^h) = \frac{1}{2} \int_{\mathcal{B}_{0e}} (x_{2e}^h - x_{2e}^{mh})^2 dV_e + \frac{\alpha}{2} \int_{\mathcal{B}_{0e}} (\mu_e^h - \mu_e^{*h})^2 dV_e, \quad (22)$$

where x_{2e}^h depending the shear modulus distribution denotes the computed deformation in axial direction, x_{2e}^{mh} is its measured counterpart, μ_e^h represents the unknown shear modulus in element e and μ_e^{*h} is a reference shear modulus. Although not mandatory, it is assumed that the shear modulus is constant within each finite element.

Minimization of functional (21) by means of the L-BFGS-B algorithm (see [4, 47]) requires the computation of \mathfrak{g} , together with its gradient. Considering element e , the gradient of \mathfrak{g} with respect to the shear modulus can be written as

$$\begin{aligned} \Delta^{\mu_e^h} \mathfrak{g}_e^h &= D_{\mu_e^h} \mathfrak{g}_e^h \cdot \Delta \mu_e^h \\ &= \int_{\mathcal{B}_{0e}} (x_{2e}^h - x_{2e}^{mh}) (\Delta^{\mu_e^h} x_{2e}^h) dV_e + \alpha \int_{\mathcal{B}_{0e}} (\mu_e^h - \mu_e^{*h}) \Delta \mu_e^h dV_e. \end{aligned} \quad (23)$$

According to (23), the sensitivity of the deformation with respect to the shear modulus distribution $\Delta^{\mu^h} x_{2e}^h$ has to be determined. It can be computed by linearizing the weak form of equilibrium (13). Finally, the gradient $D_\mu \mathbf{g}$ is derived by a classical assembling procedure combined with the adjoint method proposed in [28, 29]. In line with the forward problem, the resulting system of equations is solved by the solver PARDISO 3.2, cf. [36, 37]. Further details are omitted here. They can be found in [2].

4 Fundamentals of variational h -adaption

In this subsection, a concise review of the variational h -adaption and the clustering technique as proposed in [2] is given. The purpose of this section is twofold. First, it provides the preliminaries necessary for a better understanding of the novel variational r -adaption discussed in section 5. Secondly, the previously published efficient variational h -adaption and the novel r -adaptive scheme will finally be combined leading to a further speed-up in computing time.

As already shown in [2], the numerical computation of the inverse problem as described in the previous section is usually very time-consuming. An effective way for reducing the computing time, while maintaining or improving the quality of the numerical solution is provided by adaptive finite element meshes, cf. [1, 45], i.e., regions showing a nearly constant shear modulus distribution should efficiently be approximated by a small number of finite elements, while domains exhibiting strong gradients should be refined. Within the adaptive h -adaption advocated in [2], the inverse problem of hyperelasticity is first solved by using a relatively coarse finite element triangulation. Subsequently, regions of interest are locally refined. For that purpose, Rivara's algorithm based on the so-called *Longest-Edge-Propagation-Path* (LEPP) is applied, cf. [34, 35]. An illustration of this algorithm is depicted in figure 2.

The only critical step within the aforementioned adaptive scheme is the selection of elements to be refined. The error indicator proposed in [2] relies directly on the variational structure of the underlying mechanical problem. More precisely, denoting the spaces of admissible shear modulus distributions associated with the two different finite element triangulations \mathcal{T}_0 and \mathcal{T}_1 as $V_0^{h_\mu}$ and $V_1^{h_\mu}$, mesh \mathcal{T}_1 is better than mesh \mathcal{T}_0 if and only if, inequality

$$\inf_{\mu \in V_1^{h_\mu}} \mathbf{g}(\mu) \leq \inf_{\mu \in V_0^{h_\mu}} \mathbf{g}(\mu) \quad (24)$$

is fulfilled and thus, the error corresponding to discretization \mathcal{T}_1 is lower. Consequently, if \mathcal{T}_i is some initial mesh and \mathcal{T}_{i+1} is its local refinement generated by means of applying Rivara's LEPP algorithm to element j , a suitable error indicator can be defined as

$$\Delta \mathbf{g}_j^{\text{ref}} = \inf \mathbf{g}(\mathcal{T}_i) - \inf \mathbf{g}(\mathcal{T}_{i+1, e=j}) \quad \text{with} \quad \mathcal{T}_i \subset \mathcal{T}_{i+1, e=j}. \quad (25)$$

Accordingly, the error indicator $\Delta \mathbf{g}_j^{\text{ref}}$ measures the influence of the local refinement of element j on the function to be minimized. It bears emphasis that Rivara's LEPP algorithm yields a nested family of triangulations, i.e., $\mathcal{T}_i \subset \mathcal{T}_{i+1, e=j}$ and thus, the error indicator (25) is indeed non-negative.

A negative feature of the aforementioned mathematically and physically elegant error indicator is its efficiency: For each element within the triangulation, a global optimization problem has to be solved showing the same numerical complexity as the original inverse

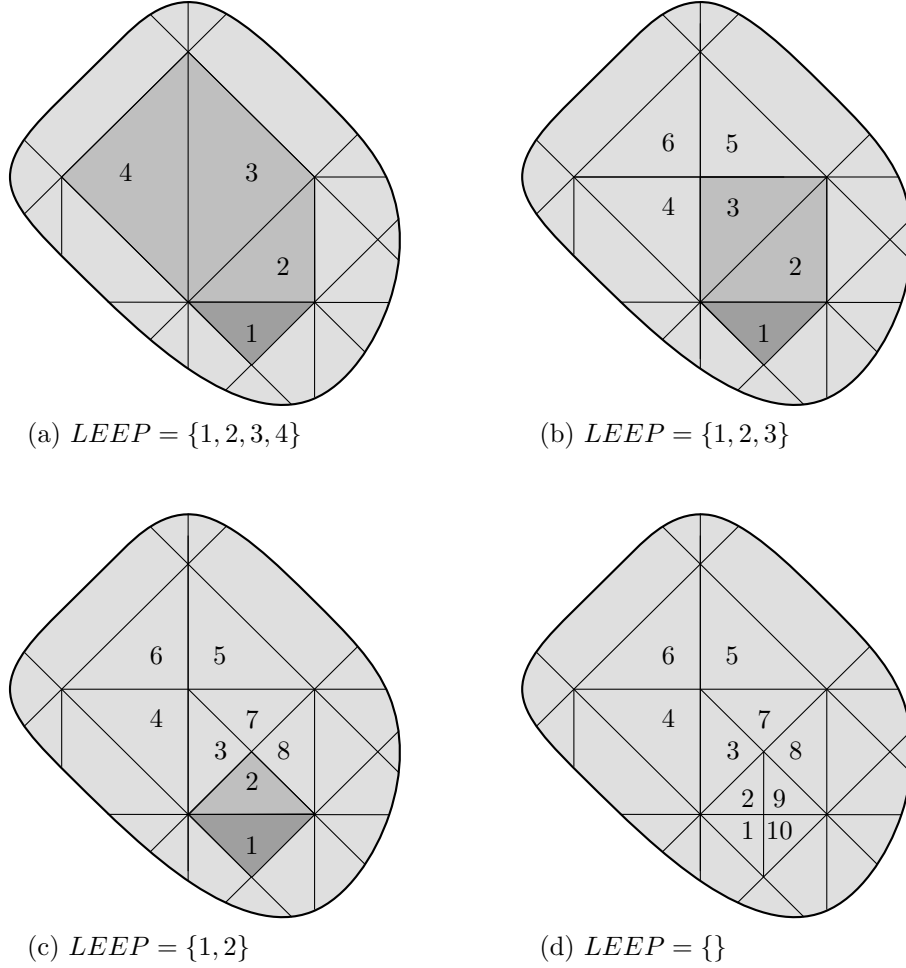


Figure 2: LEPP-algorithm according to Rivara, cf. [34, 35]: Suppose element 1 is to be refined. In this case, the LEPP of element 1 is determined and the so-called *terminate* triangle element (4) is subdivided by cutting its longest edge. This procedure is repeated until element 1 is finally refined. *Definition of LEPP*: The LEPP of a triangle is the ordered list of all triangles such that t_i is the neighbor triangle of t_{i-1} by the longest side.

problem. For this reason, the conservative estimate

$$\begin{aligned}
0 \leq \Delta \bar{\mathbf{g}}_j^{\text{ref}} := & \inf_{\mu_i^h \in V_i^{h\mu}} \mathbf{g}^h(\mathcal{T}_i) \\
- & \inf_{\substack{\mu_{i+1}^h \in V_{i+1, e=j}^{h\mu} \\ \text{supp}(\mu_{i+1}^h - \mu_i^h) = \text{supp}(V_{i+1, e=j}^{h\mu} / V_i^{h\mu})}} \mathbf{g}^h(\mathcal{T}_{i+1, e=j}) \leq \Delta \mathbf{g}_j^{\text{ref}} \quad (26)
\end{aligned}$$

was introduced in [2]. In sharp contrast to error indicator (25), $\Delta \bar{\mathbf{g}}_j^{\text{ref}}$ compares the objective function of the initial discretization to a partially, locally relaxed solution. This solution is obtained by re-computing the shear modulus distribution of the refined mesh only within the refined elements. Evidently, this leads to an upper bound of the completely relaxed energy and hence, $\Delta \bar{\mathbf{g}}_j^{\text{ref}} \leq \Delta \mathbf{g}_j^{\text{ref}}$. Furthermore, since the number of newly refined elements is significantly smaller than the total number of elements, the error indicator (26) is very efficient. Equally importantly, the number of new elements as generated by applying Rivara's LEPP algorithm to a certain element is almost independent of the original discretization and as a result, the numerical complexity of the overall algorithm

is $\mathcal{O}(n)$.

Remark 4.1 *It is important to note that classical error estimates such as those described in [1, 45] cannot be used for the inverse problem of hyperelasticity, since they require linearity of the underlying Hilbert space, cf. [5]. Clearly, this condition is not met here. However, it should also be noted that the refinement criterion used in the present paper and originally proposed in [2] is mathematically speaking not an error estimate, but only an error indicator. Although not being an error estimate, the variational error indicator guarantees indeed that only those elements are refined which lead to an improvement of the solution. This is in sharp contrast to other error indicators which are purely heuristic in nature. Furthermore, if the objective function to be minimized was quadratic as for the forward problem of linearized elasticity theory, the variational error indicator would be an estimate. Further details on the mathematical properties of the variational mesh adaptation can be found in [25, 26].*

Remark 4.2 *In [2], the aforementioned variational h -adaptation was combined with a clustering technique similar to that used in digital image compression. Since this clustering will also be applied within the present paper, it will be briefly discussed here. Its fundamental idea is the arranging of the elements' shear moduli into m intervals. Within each of these intervals, the same shear modulus is assigned to all elements. Consequently, if m is chosen as significantly less than the total number of elements, the procedure is indeed a compression and thus, it reduces the number of degrees of freedom and increases the efficiency of the resulting numerical scheme. Further details on the clustering technique can be found in [2].*

5 Variational r -adaptation

A careful analysis of the h -adaptation reveals that, although it is very promising for enriching the finite element space, it is not the most efficient method for detecting interfaces within the material (see figure 1). For that purpose, a novel variationally consistent r -adaptive scheme is elaborated here. Conceptually, the nodal coordinates defining the finite element triangulation are optimized. Such a method has already been successfully applied to the forward problem discretized by standard displacement-driven finite elements, cf. [3, 21, 25, 43] (see also [11, 23]). It is closely related to classical Eshelby mechanics in which the deformation of material defects such as internal interfaces is studied, see [9, 10]. In the present paper, the method originally advocated in [3, 21, 25, 43] is extended in two directions. First, since quasi-incompressible materials are considered, the r -adaptation has to be combined with a mixed finite element formulation. Secondly and equally importantly, it is elaborated for the inverse problem.

5.1 Fundamentals

The underlying idea of the novel variationally consistent r -adaptation is very natural: Since the function to be minimized (19) depends implicitly on a finite element discretization, which in turn, depends on the nodal coordinates $\mathbf{X}^h = \mathbf{X}^h(\mathbf{X}^I)$ of the undeformed configuration, it is canonical to optimize (19) with respect to both the shear moduli μ^h and the nodal coordinates $\mathbf{X}^h(\mathbf{X}^I)$. More precisely, the slightly modified function

$$\mathfrak{h}^h(\mu^h, \mathbf{X}^h) = \mathfrak{g}^h(\mu^h, \mathbf{X}^h) + \tilde{\alpha} \mathfrak{h}_{\text{geo}}(\mathbf{X}^h) \quad (27)$$

is minimized. While the first term in (27) has already been extensively discussed in section 3, the term $\mathfrak{h}_{\text{geo}}(\mathbf{X}^h)$ is associated with the shape of the finite elements within the triangulation. More precisely, it defines a geometrical shape measure according to [12, 19, 20] attaining its minimum, if all finite elements show an almost ideal shape (angles between elements' edges are 60°), while for degenerating elements (one angle between elements' edges converges to 0°) it approaches infinity. Consequently, a minimization of $\mathfrak{h}_{\text{geo}}(\mathbf{X}^h)$ will lead to a triangulation having elements with relatively small aspect ratios. It is noteworthy that this criterion is equivalent to minimizing the interpolation error. Further details can be found in B (see also Remark 5.1). Clearly, the variational r -adaption should result in a finite element mesh capturing material interfaces well. The geometrical shape measure is only introduced for avoiding degenerated elements. Thus, the scalar weighting coefficient $\tilde{\alpha}$ has to be chosen as small as possible.

In line with the implementation of the inverse problem of elasticity imaging (see section 3), the L-BFGS-B algorithm is also utilized for solving Problem (27). Since the gradient of the objective function with respect to the elements' shear moduli has already been given in section 3 (see (23)), only the sensitivity of $\mathfrak{h}^h(\mu^h, \mathbf{X}^h)$ with respect to the reference configuration \mathbf{X}^h (more precisely, the nodal coordinates \mathbf{X}^I) remains to be derived, i.e., $D_{\mathbf{X}^h} \mathfrak{h}^h(\mu^h, \mathbf{X}^h)$. By applying the finite element method leading to

$$\mathfrak{h}^h(\mu^h, \mathbf{X}^h) = \sum_{e=1}^{n_e} \mathfrak{h}_e^h(\mu_e^h, \mathbf{X}_e^h) \quad (28)$$

with

$$\mathfrak{h}_e^h(\mu_e^h, \mathbf{X}_e^h) = \frac{1}{2} \int_{\mathcal{B}_{0e}} (x_{2e}^h - x_{2e}^{\text{mh}})^2 \, dV_e + \frac{\alpha}{2} \int_{\mathcal{B}_{0e}} (\mu_e^h - \mu_e^{*h})^2 \, dV_e + \tilde{\alpha} \mathfrak{h}_{\text{geo}_e} \quad (29)$$

this linearization follows from the assembly of the elements' sensitivities. Based on (29) they are obtained as

$$\begin{aligned} \Delta^{\mathbf{X}^h} \mathfrak{h}_e^h(\mu_e^h, \mathbf{X}_e^h) &= \int_{\mathcal{B}_{0e}} (x_{2e}^h - x_{2e}^{\text{mh}}) \left(\Delta^{\mathbf{X}^h} x_{2e}^h - \Delta^{\mathbf{X}^h} x_{2e}^{\text{mh}} \right) \, dV_e \\ &+ \frac{1}{2} \int_{\mathcal{B}_\xi} (x_{2e}^h - x_{2e}^{\text{mh}})^2 \, D_{\mathbf{X}^h} (\det \mathbf{F}_{\hat{\Phi}}) \cdot \Delta \mathbf{X}_e^h \, dV_\xi \\ &+ \alpha \int_{\mathcal{B}_{0e}} (\mu_e^h - \mu_e^{*h}) \Delta^{\mathbf{X}^h} \mu_e^h \, dV_e + \tilde{\alpha} [D_{\mathbf{X}^h} (\mathfrak{h}_{\text{geo}_e}) \cdot \Delta \mathbf{X}_e^h] . \end{aligned} \quad (30)$$

Here, the dependence of x_{2e}^h on the reference configuration has already been considered ($\mathbf{x}^h = \mathbf{x}^h(\mathbf{X}^h) = \mathbf{x}^h(\mathbf{X}^I)$). For the derivation of (30), it is convenient to distinguish strictly between the undeformed \mathcal{B}_0 and the deformed configuration \mathcal{B}_t and to introduce the additional so-called *reference domain* \mathcal{B}_ξ parametrized in terms of the natural coordinates $\boldsymbol{\xi}$. This third domain, although usually implicitly used in finite element methods, is often not explicitly highlighted. The connections between the three aforementioned configurations is shown in figure 3. Accordingly, two independent mappings are necessary: While $\hat{\Phi}$ connects points within the reference domain \mathcal{B}_ξ to their counterparts in the material configuration \mathcal{B}_0 , $\bar{\Phi}$ relates the reference domain \mathcal{B}_ξ to the deformed configuration \mathcal{B}_t . Thus, the physical deformation φ can be understood as a composition of the type $\varphi = \bar{\Phi} \circ \hat{\Phi}^{-1}$ and the deformation gradient resulting from the chain rule decomposes

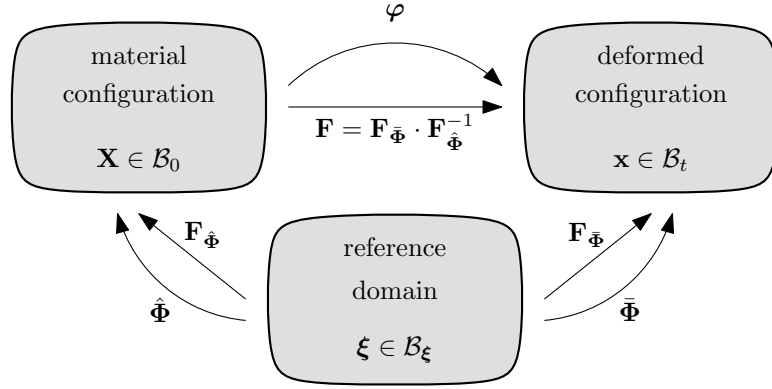


Figure 3: Different configurations and mappings characterizing *Arbitrary Lagrangian Eulerian formulations* (ALE) kinematics

multiplicatively, i.e.,

$$\mathbf{F} = \mathbf{F}_{\hat{\Phi}} \cdot \mathbf{F}_{\hat{\Phi}}^{-1} \quad \text{with} \quad \mathbf{F}_{\bar{\Phi}} = \frac{\partial \bar{\Phi}}{\partial \boldsymbol{\xi}} \quad \text{and} \quad \mathbf{F}_{\hat{\Phi}} = \frac{\partial \hat{\Phi}}{\partial \boldsymbol{\xi}}. \quad (31)$$

Analogously to standard finite elements, the mappings $\bar{\Phi}$ and $\hat{\Phi}$ are approximated by standard shape functions, i.e., by (14). According to figure 3, the arbitrary Lagrangian-Eulerian (ALE) kinematics is formally identical to that of finite strain plasticity theory and the deformation mapping φ depends on the nodal variables \mathbf{x}^I as well as on \mathbf{X}^I , i.e., $\varphi(\mathbf{x}^I, \mathbf{X}^I)$. Having in mind that \mathbf{x}^h and \mathbf{X}^h are interpolated by the nodal quantities \mathbf{x}^I and \mathbf{X}^I , φ will be sometimes written as $\varphi = \varphi(\mathbf{x}^h, \mathbf{X}^h)$. Although this notation is strictly speaking not completely correct, since \mathbf{x}^h is also the approximation of φ , it is more compact. If at a certain point danger of confusion exists, additional comments will be added.

Since a staggered solution scheme is employed in what follows, i.e., the computation of the shear modulus distribution and the optimization of the nodal coordinates are not performed simultaneously but one after another, the Tikhonov-type regularization is not required within the r -adaption step. Consequently and for the sake of efficiency, the next to last term in (30) will not be considered anymore. However, it could be taken into account in a straightforward manner. For this reason, the linearization (30) of the objective function requires only three terms. The first of those is associated with the sensitivities of the numerically predicted deformation $\Delta^{\mathbf{X}^h} x_{2e}^h$ and its measured counterpart $\Delta^{\mathbf{X}^h} x_{2e}^{mh}$. The second term is related to the change in volume due to a variation of the nodal coordinates defining the undeformed configuration. The final term corresponds to the penalty function $\mathfrak{g}_{\text{geo}_e}$. It can be found in B.

The sensitivity $\Delta^{\mathbf{X}^h} x_{2e}^h$ is computed by linearizing the weak form of equilibrium (12) with respect to \mathbf{X}^h . Considering element e leads to

$$\boldsymbol{\eta}_x^I \cdot \mathbf{K}_e^{\Delta \mathbf{x}^{IJ}} \cdot \Delta^{\mathbf{X}^J} \mathbf{x} + \boldsymbol{\eta}_x^I \cdot \mathbf{K}_e^{\Delta \mathbf{X}^{IJ}} \cdot \Delta \mathbf{X}^J = 0, \quad (32)$$

where $\mathbf{K}_e^{\Delta \mathbf{x}^{IJ}}$ is the classical element stiffness matrix, see [2]. The second stiffness matrix $\mathbf{K}_e^{\Delta \mathbf{X}^{IJ}}$ is not standard. It describes the sensitivities of the vector of residual forces with respect to the coordinates \mathbf{X}^h of the underlying discretization. A compact summary of its derivation is presented in A. The assembling of (32) yields finally

$$[\Delta^{\mathbf{X}} \mathbf{x}] = -[\mathbf{K}^{\Delta \mathbf{x}}]^{-1} [\mathbf{K}^{\Delta \mathbf{X}}] [\Delta \mathbf{X}] = [\mathbf{S}] [\Delta \mathbf{X}] \quad (33)$$

or equivalently

$$[\mathbf{K}^{\Delta \mathbf{x}}][\mathbf{S}] = -[\mathbf{K}^{\Delta \mathbf{X}}]. \quad (34)$$

Analogously to the algorithm for the inverse problem of elasticity imaging and in line with [28, 29], the adjoint method is used for reducing the numerical costs corresponding to the computation of $[\Delta^{\mathbf{X}^h} \mathbf{x}]$, i.e., (34) is not solved directly. More precisely, the notations

$$T_{1e}^I = \int_{\mathcal{B}_0^e} (x_{2e}^h - x_{2e}^{mh}) N_I^\varphi \, dV_e \quad \text{and} \quad (35)$$

$$T_{2ei}^I = \frac{1}{2} \int_{\mathcal{B}_0^e} (x_{2e}^h - x_{2e}^{mh})^2 F_{\hat{\Phi}ji}^{-1} \frac{\partial N_I^\varphi}{\partial \xi_j} \, dV_e, \quad (36)$$

together with their assembled global counterparts $[\mathbf{T}_1]$ and $[\mathbf{T}_2]$,

$$[\mathbf{w}] := -[\mathbf{K}^{\Delta \mathbf{x}}]^{-1}[\mathbf{T}_1] \quad (37)$$

are introduced instead. Clearly, computing $[\mathbf{w}]$ is significantly more efficient than solving (34) for $[\mathbf{S}]$. Inserting (35)–(37) into the assembled version of (30) and considering the Schwarz’s theorem, the gradient of the objective function with respect to the nodal coordinates is obtained as

$$[\Delta^{\mathbf{X}^h} \mathfrak{h}] = ([\mathbf{w}][\mathbf{K}^{\Delta \mathbf{x}}] - [\mathbf{T}_1][\mathbf{S}^m] + [\mathbf{T}_2] + [\mathbf{D}_{\mathbf{X}^h} \mathfrak{h}_{\text{geo}}]) [\Delta^{\mathbf{X}^h}]. \quad (38)$$

The sensitivity $\Delta^{\mathbf{X}^h} x_{2e}^{mh}$ describing the change of the measured deformation depending on a variation applied to the nodal coordinates of the undeformed configuration, is given by

$$\Delta^{\mathbf{X}^k} x_{2k}^{mh} = \mathbf{D}_{\mathbf{X}}(x_{2k}^{mh}) \cdot \Delta \mathbf{X}^k = \mathbf{S}^m_k \cdot \Delta \mathbf{X}^k. \quad (39)$$

A relatively straightforward computation yields the node contribution

$$\mathbf{S}^m_k = \frac{\partial N_J^\varphi}{\partial \xi} \cdot \mathbf{F}_{\hat{\Phi}}^{-1} x_{2J}^{gT_m} \quad (40)$$

which can be assembled to the global matrix $[\mathbf{S}^m]$. Here, $x_{2J}^{gT_m}$ is the deformation field at node J within the grid defining the measured data. Note that $[\mathbf{S}^m]$ shows a pronounced diagonal structure.

Remark 5.1 *Function (27) to be optimized depends on two terms. As already mentioned, the first of those is related to the error between measured and numerically computed deformation, while the second corresponds to a geometrical shape measure and avoids degenerated elements (large aspect ratios). Interestingly, considered hyperelastic material model shows already an intrinsic geometrical shape measure. For showing this, an element which degenerates is considered. In this case, continuity implies $\det \mathbf{F}_{\hat{\Phi}} \rightarrow 0$, and consequently, $\det \mathbf{F} \rightarrow 0$. Accordingly, $U(J) \rightarrow \infty$ (see (4)) and thus, the total potential energy converges to infinity as well. As a result, if minimization is the overriding principle (as in the advocated approach), degenerated elements are energetically not favorable and cannot occur. However, since the geometrical shape measure $\mathfrak{g}_{\text{geo}_e}$ stabilizes the numerical method additionally, it is nevertheless employed.*

Remark 5.2 *The advocated scheme is a staggered method, i.e., a minimization with respect to the shear moduli is considered first. Subsequently, the nodal positions defining the finite element triangulations are optimized. However, by combining the gradients with respect to the shear moduli and those related to nodal positions, a monolithic scheme can be derived in a straightforward manner. The proposed scheme has been chosen, since it allows using the same subroutines originally developed for the standard inverse problem.*

Remark 5.3 *The proposed r -adaptive algorithm is based on an L -BFGS- B algorithm. The stability and convergence properties of this algorithm can be found, e.g., in [4, 47]. However, convergence of the numerical scheme can be easily verified directly: Each of the two steps defining the staggered scheme decreases the function to be minimized. Hence, combining both steps leads to a monotonically decreasing sequence. Furthermore, the function to be minimized is bounded below by zero. It is well known that any monotonically decreasing sequence which is bounded below converges.*

Remark 5.4 *As mentioned before, the parameter $\bar{\alpha}$ is required for avoiding degenerated finite elements. However, if this parameter is too large, elements showing edges with the same length will be preferred and thus, the nodes do not move according to the distribution of the shear modulus. Therefore, this parameter has to be chosen as small as possible. Within the numerical examples, $\bar{\alpha}$ has been determined by hand. More precisely, the convergence rate of the L -BFGS- B algorithm during the first iteration steps was monitored. Starting with zero, $\bar{\alpha}$ was successively increased until a good convergence rate has been observed. Alternatively, a mathematically more rigorous definition of $\bar{\alpha}$ can be derived based on the Hessian matrix of the function to be minimized. According to [24], $\bar{\alpha}$ has to be chosen such that the Hessian is positive definite.*

5.2 Numerical example

For analyzing the performance of the novel variationally consistent r -adaptation, two different examples are considered. The first of those is depicted in figure 4. It is characterized by one inclusion embedded within a softer matrix. The shear modulus of the inclusion is set to $\mu_{\text{inc}} = 50$ kPa and that of the surrounding material to $\mu_{\text{mat}} = 10$ kPa. Incompressibility is approximated by setting the Poisson's ratio to $\nu = 0.48$.

The initial discretization of the variational r -adaptation is shown in figure 5(a). Accordingly, this triangulation is significantly coarser than that characterizing the forward problem (see figure 4). Furthermore, the edges of the finite elements are not aligned with the boundary of the inclusion. Consequently, the initially assumed shape of the inclusion is different to that of the forward problem. For showing exclusively the effect of the proposed r -adaptation, the shear moduli within the inclusion and the surrounding material are kept fixed. Such moduli are chosen in line with the forward problem. Thus, only the nodal positions are unknowns. By doing so, the effect of the standard inverse algorithm for computing the shear moduli can be excluded.

The results predicted by the proposed r -adaptive algorithm are illustrated in figure 5. The parameter $\bar{\alpha}$ used for enforcing small aspect ratios of the finite elements is set to

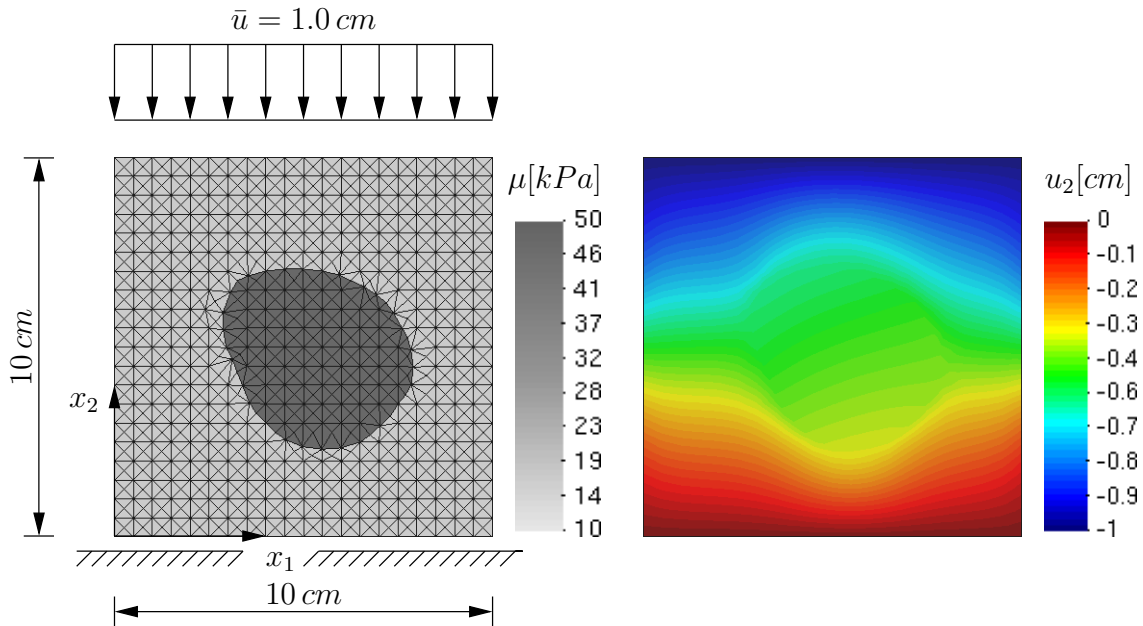


Figure 4: Numerical compression test of biological tissue with one hard lump: (a) geometry, distribution of the shear modulus and boundary conditions, (b) computed displacement field (forward problem). Within the computation, the strain energy defined by (2) and (4) has been adopted.

$\tilde{\alpha} = 2 \cdot 10^{-9}$, cf. (27). According to figure 5, the topology of the inclusion is detected efficiently by the novel algorithm. Already after five iteration steps, the topology of the inclusion is well reproduced by moving the nodes of the underlying finite element discretization. In summary and as expected, the interfaces between different materials can be effectively captured by r-adaption – particularly, compared to h-adaption. More precisely, a significantly finer discretization would have been required for getting similar results by using the h-adaptive method. However it bears emphasis that even if the material interfaces are capture qualitatively by small elements, an alignment between the elements’ edges and the material interface can never be guaranteed by h-adaptivity. This is a fundamental difference compared to r-adaptivity.

Next, the performance of the fully coupled r-adaptive algorithm is analyzed. Thus and in contrast to the example considered before, the nodal positions of the underlying finite element discretization as well as the shear moduli within the finite elements are optimized. For analyzing the coupled r-adaptive scheme, the deformation field predicted by the forward problem in figure 6 is utilized as artificial experiment data. The ratio of the inclusion’s shear modulus to that of the surrounding material is $\mu_{\text{inc}}/\mu_{\text{mat}} = 5/1$. Starting from a uniform finite element mesh and assuming a spatially constant shear modulus, the inverse problem of hyperelasticity is subsequently solved numerically. Finally, the proposed *r*-adaption is applied. For reducing the numerical costs associated with this algorithm, the triangulation corresponding to the undeformed configuration is interpolated in an elementwise linear fashion (in contrast to the deformed configuration which is interpolated piecewise quadratically). Within all computations, the weighting factor $\tilde{\alpha}$ was set to $\tilde{\alpha} = 2 \cdot 10^{-9}$.

The results (relative stiffness distributions) computed for different uniform finite element triangulations are illustrated in figure 7 left. As expected and as already presented

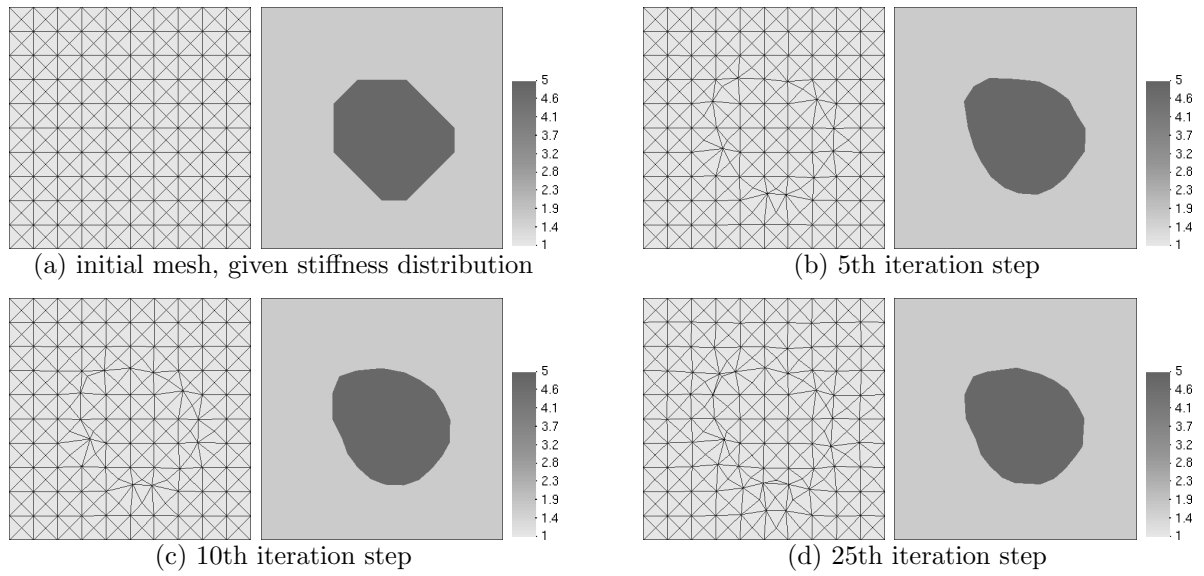


Figure 5: Results of the variational r-adaptation (compare to the underlying the forward problem illustrated in figure 4): mesh and shear modulus distribution for different iteration steps. The shear moduli have been fixed within all computations. Thus, only the nodal positions of the finite element triangulation have been computed.

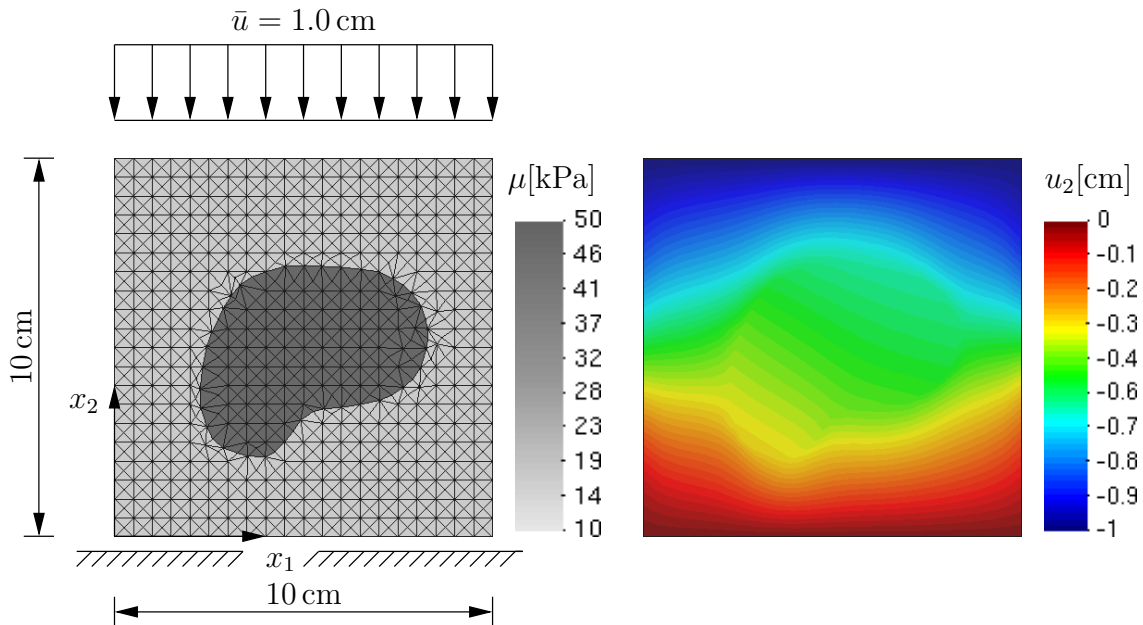


Figure 6: Numerical compression test of biological tissue with one hard lump: (a) geometry, distribution of the shear modulus and boundary conditions, (b) computed displacement field (forward problem). Within the computation, the strain energy defined by (2) and (4) has been adopted.

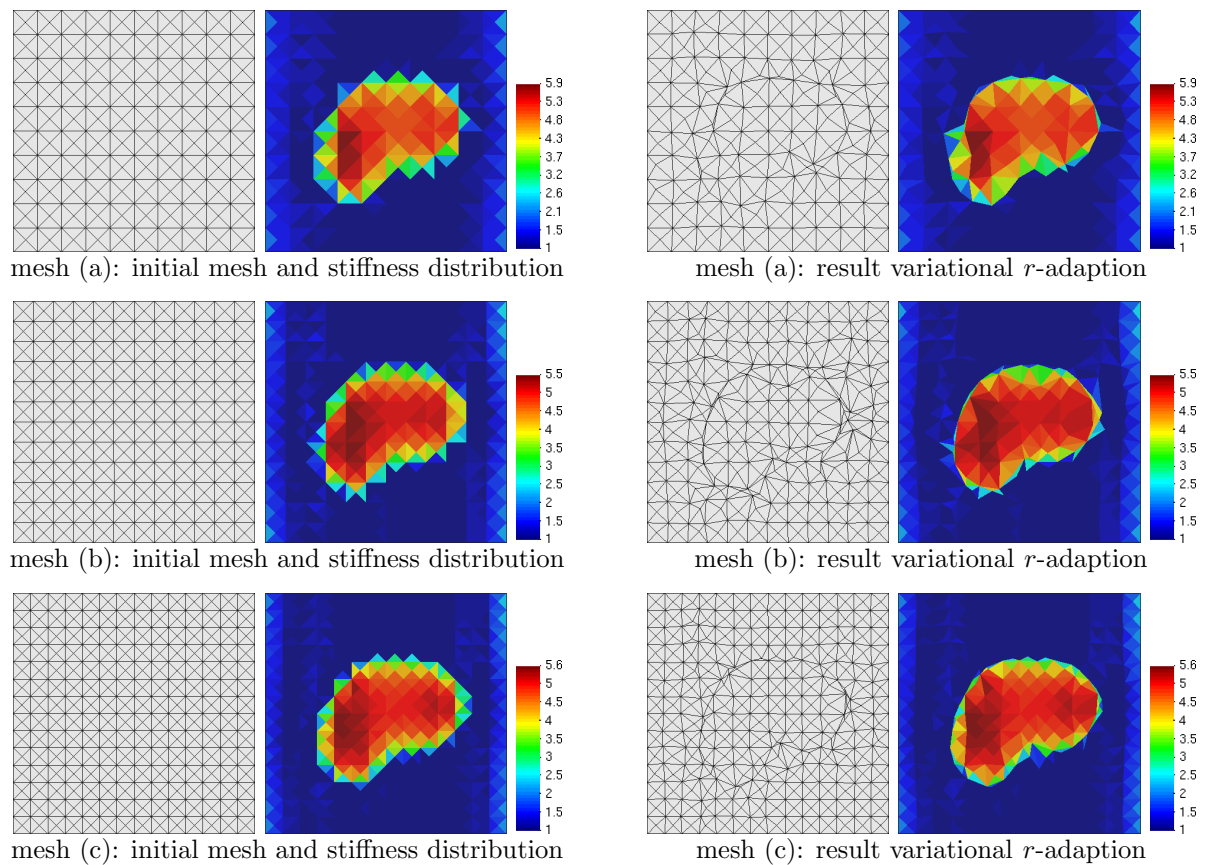


Figure 7: Stiffness distributions as predicted by the inverse problem of hyperelasticity for different triangulations (compare to the underlying forward problem in figure 6): Left: homogeneous discretizations. Right: After applying the proposed r -adaption to the homogeneous meshes on the left side

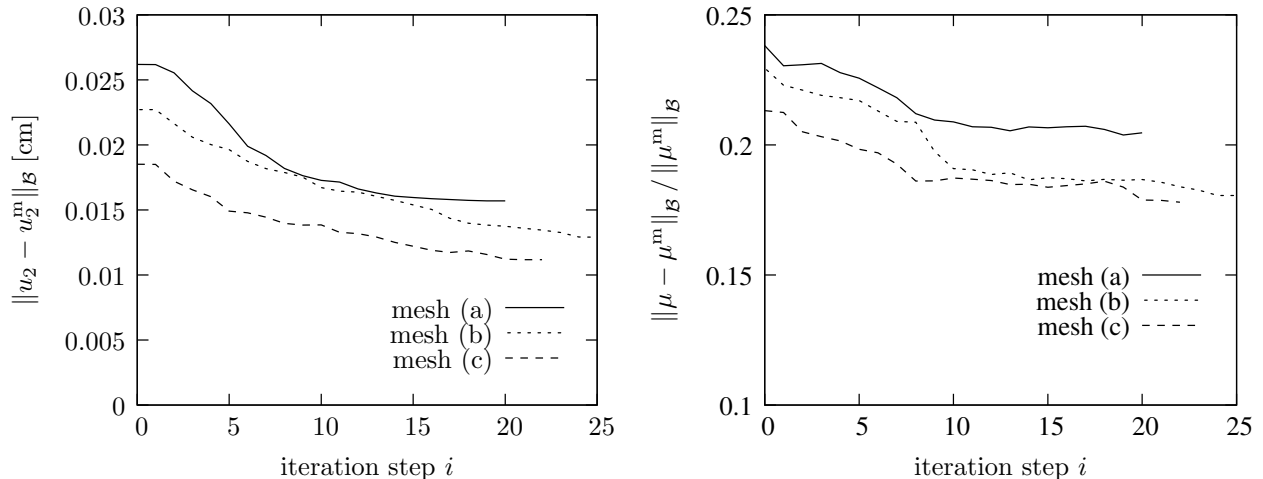


Figure 8: Evolution of displacement and shear modulus errors for the variational r -adaption depending on the iteration step within the optimization algorithm (compare to figure 7)

in [2], the accuracy of the solution increases with an increasing number of elements. The same holds for the novel r -adaption (see figure 7 right). Furthermore and even more importantly, the r -adaption indeed captures the material interface significantly better and thus, leads to an improved solution. The small numerical artefacts in figure 7 could be further reduced by using a smaller tolerance within the L-BFGS-B algorithm and by applying a smoothing procedure to the distribution of the shear moduli. However, it bears emphasis that the exact solution cannot be expected, since the underlying mesh of the r -adaption is significantly coarser than that defining the forward problem.

The improvement of the solution due to r -adaption can be seen better by analyzing the errors

$$\epsilon_u = \|u_2 - u_2^m\| \quad \text{and} \quad \epsilon_\mu = \|\mu - \mu^m\| / \|\mu^m\|. \quad (41)$$

Both of them are based on the L_2 norm. According to figure 8, the proposed adaptive finite element method indeed leads to more accurate results. More precisely, it can be seen that both errors converge monotonically. This is a direct consequence of the variational consistency of the method.

6 hr -adaption in elasticity imaging

The variationally consistent r -adaption discussed in the previous section requires only a relatively coarse triangulation for detecting material interfaces. As a consequence, the resulting approach is numerically very efficient. However, a coarse mesh also implies that the underlying finite element spaces associated with the deformation mapping are relatively small and thus, they are usually not rich enough for predicting the deformation field sufficiently accurately (the forward problem). For this reason, the novel variational r -refinement is combined with the variational h -adaption [2] to obtain a variational hr -refinement algorithm. The resulting approach captures material interfaces well (by using r -adaption) and predicts a deformation field in good agreement with that observed experimentally (by using h -adaption).

6.1 Numerical example

In this subsection, the performance of the novel hr -adaptive finite element formulation is highlighted by means of numerical analyses of the forward problem shown in figure 6. More precisely, the deformation field as predicted by the forward problem in figure 6 serves again as an artificial experiment. The respective data are used within the inverse problem of hyperelasticity, which in turn, is solved by applying the novel hr -adaption. Since the deformation mapping corresponding to the forward problem is relatively smooth compared to measured data containing some noise, different noise levels are considered as well (0.5% and 2.0%; normal distribution).

As evident, the variationally consistent r -adaption and the respective h -refinement can be combined in several manners. In this subsection, the following two choices will be analyzed:

- hr -adaption: First, the h -refinement is applied and subsequently, the r -adaptive scheme is used.
- rh -adaption: First, the r -refinement is applied and subsequently, the h -adaptive scheme is used.

Within all computations, the stiffness distribution is determined first by solving the inverse problem of elasticity imaging with a comparably coarse and uniform finite element discretization (8x8 mesh). Analogously to the examples presented previously, convergence within the respective optimization algorithms is checked by the criteria $(\mathbf{g}(\mu^i) - \mathbf{g}(\mu^{i-5})) / (\mathbf{g}(\mu^{i-5})) < 0.01$ and $\mathbf{g}(\mu^i) < 1.0 \times 10^{-18}$. Having computed the stiffness distribution associated with the coarse mesh, the adaptive algorithms are subsequently employed. While the r -adaptive step is uniquely defined, the h -refinement requires some further explanations. Here, 15% of the elements showing the largest variational error indicator (26), are refined by means of Rivara's LEPP algorithm. The number of intervals utilized within the clustering technique is set to $n = 30$ (see Remark 4.2). In contrast to the classical L_2 norm, the objective function is computed by the modified norm $\|f\|_{\text{norm}} := 1/V \int_V f dV$, cf. [2].

The results of the variational hr -adaptive scheme are illustrated in figure 9. The predicted meshes and the shear modulus distributions associated with the h -refinement step are shown for different noise levels on the left hand side in figure 9. As expected, the accuracy of the scheme decreases with an increasing noise level. However, for all noise levels, the adaptive scheme improves the quality of the solution and captures the hard lump better. This can also be seen in figure 10. Accordingly, both errors (deformation and shear modulus distribution) decrease. The results of the subsequent r -adaption are presented on the right hand side in figure 9. Compared to the initial h -refinement step, they lead to a further improvement of the results. Again, the influence of the noise on the predicted shear modulus distribution is obvious. In line with the h -adaption, the variational consistency of the r -adaptive scheme guarantees and improvement of the results, see figure 10. A more careful analysis of figure 10 reveals that the impact of the h -adaption on the errors is significantly larger than that of the r -refinement method. However, it bears emphasis that the numerical costs of the h -adaptive scheme are also higher. Therefore, a reasonable comparison should take the runtime of the algorithms into account. Such a comparison will thus be presented at the end of this subsection.

The results as obtained from the rh -adaptive finite element formulation are summarized in figures 11 and 12. They are in good agreement with those of the hr -refinement scheme. More precisely, it can be seen that this method leads also to an improvement

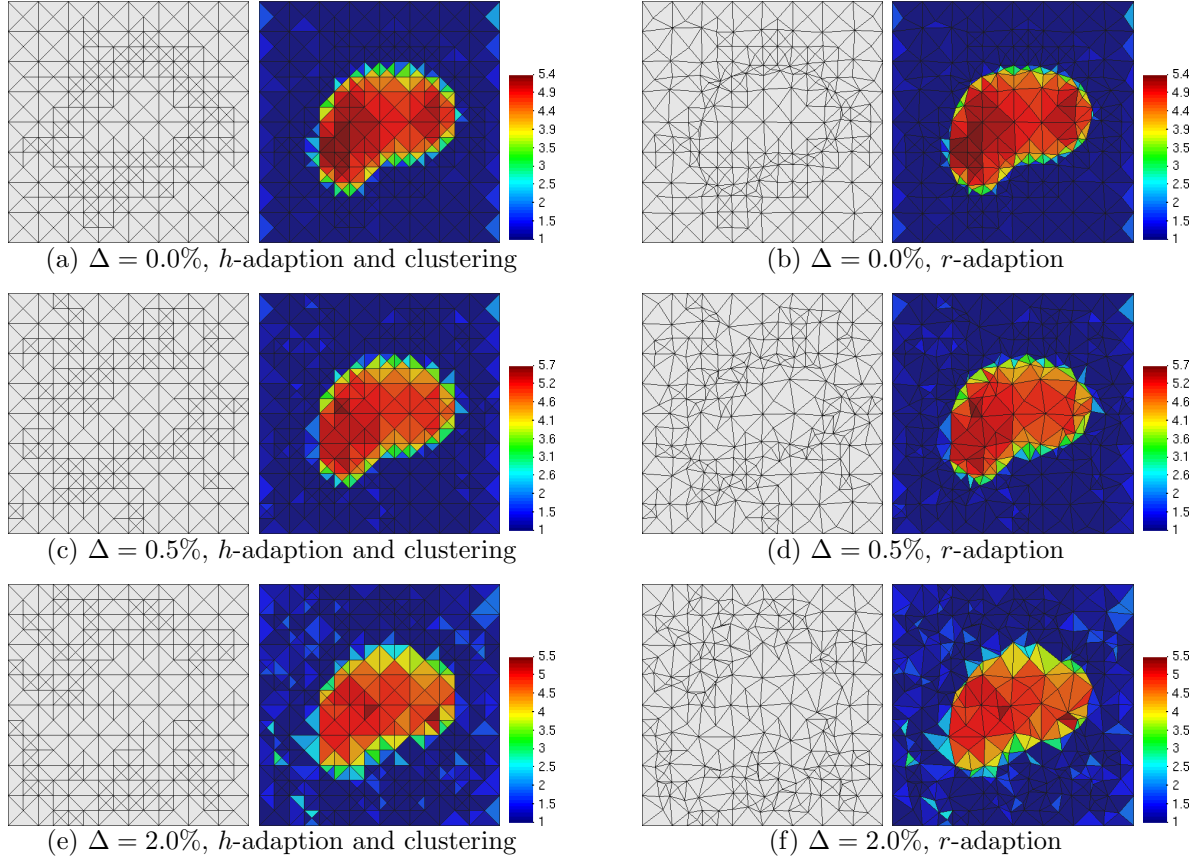


Figure 9: Compression test of biological tissue with one hard lump, cf. figure 6: Computed discretizations and shear modulus distributions: Left hand side: Results based on the variational h -adaption combined with the clustering technique; right hand side: Results of the subsequent variational r -adaption (The noise-level is denoted as Δ)

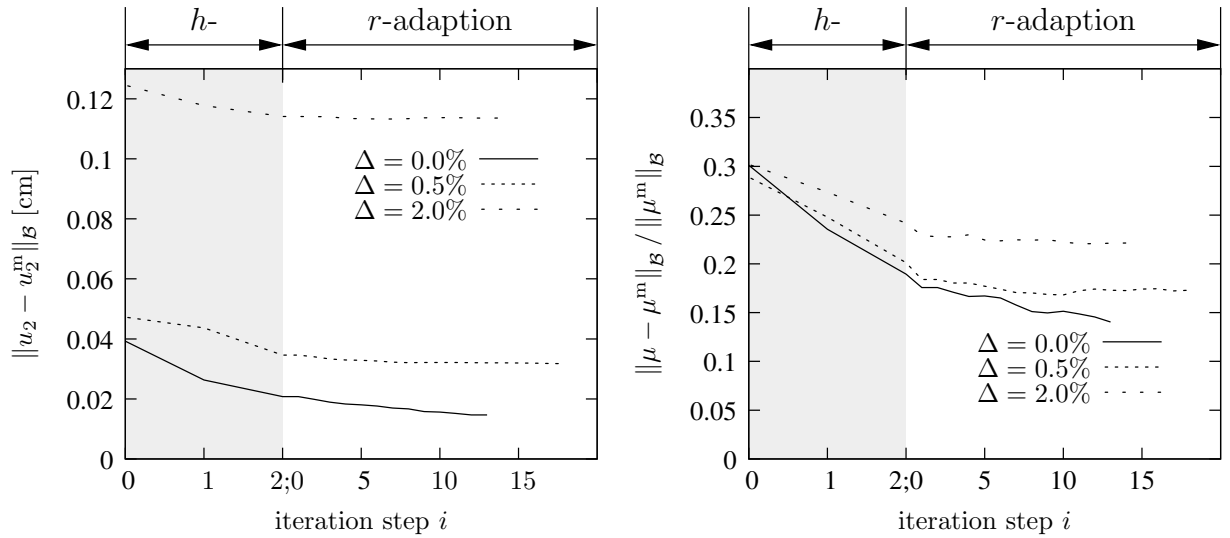


Figure 10: Compression test of biological tissue with one hard lump, cf. figure 6: Performance and accuracy of the variational hr -adaption. Left: Error in the displacement field; right: Error in the shear modulus distribution

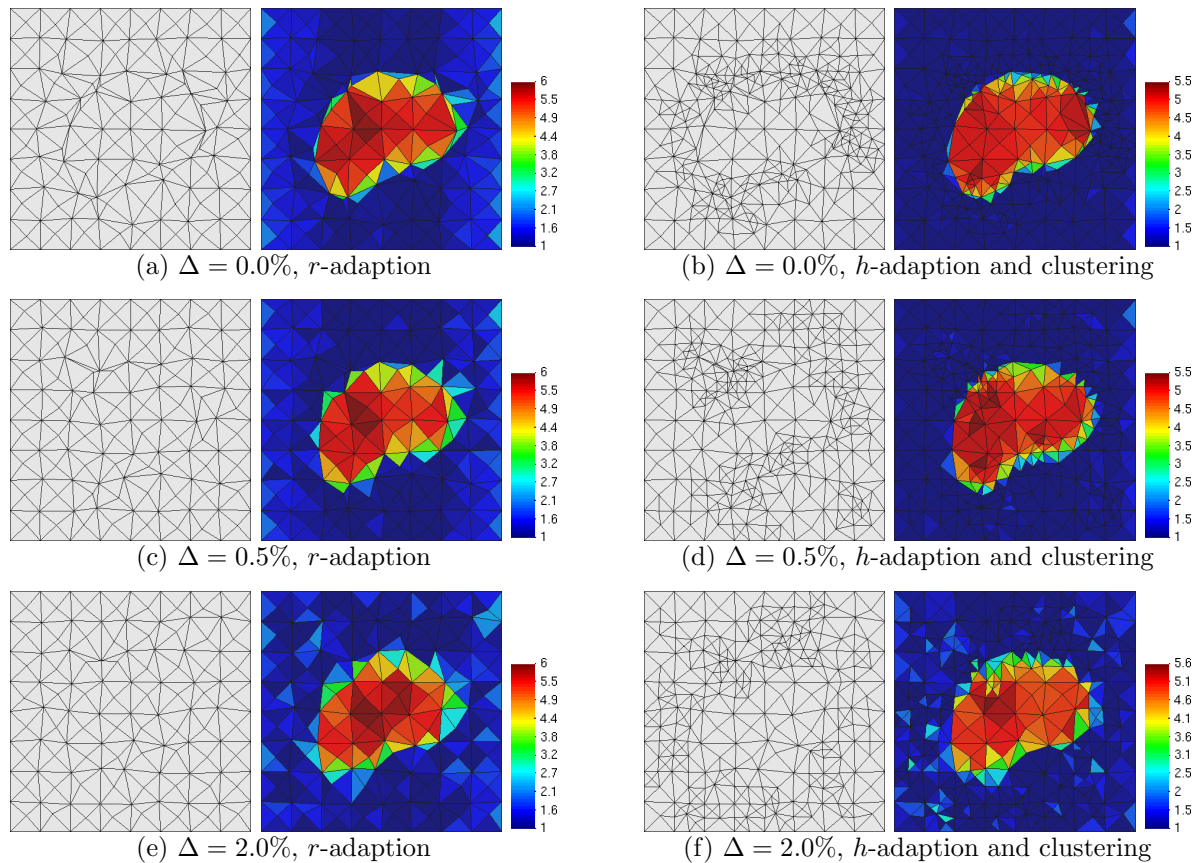


Figure 11: Compression test of biological tissue with one hard lump, cf. figure 6: Discretization and computed shear modulus distribution; Left hand side: Results based on the variational r -adaption; right hand side: Results of the subsequent variational h -adaption combined with the clustering technique; The noise-level is denoted as Δ .

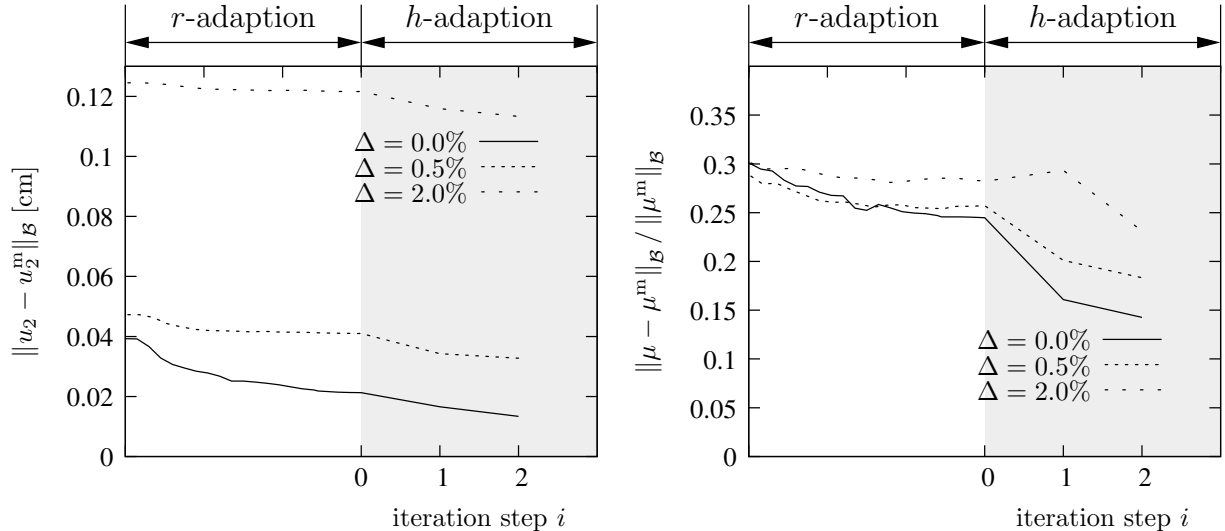


Figure 12: Compression test of biological tissue with one hard lump, cf. figure 6: Performance and accuracy of the variational rh -adaption. Left: Error in the displacement field; right: Error in the shear modulus distribution

Method	Noise level	Reg. parameter α	$\ u_2 - u_2^m\ $	$\ \mu - \mu^m\ / \ \mu^m\ $	Δt [%]
Standard	$\Delta = 0.0\%$	0.0	0.0143	0.2051	-
hr -adaptiv	$\Delta = 0.0\%$	0.0	0.0146	0.1404	32
rh -adaptiv	$\Delta = 0.0\%$	0.0	0.0134	0.1426	30
Standard	$\Delta = 0.5\%$	$7.5 \cdot 10^{-8}$	0.0311	0.2157	-
hr -adaptiv	$\Delta = 0.5\%$	$7.5 \cdot 10^{-8}$	0.0318	0.1730	14
rh -adaptiv	$\Delta = 0.5\%$	$7.5 \cdot 10^{-8}$	0.0327	0.1832	27
Standard	$\Delta = 2.0\%$	$7.5 \cdot 10^{-7}$	0.1076	0.24845	-
hr -adaptiv	$\Delta = 2.0\%$	$7.5 \cdot 10^{-7}$	0.1139	0.2217	-5
rh -adaptiv	$\Delta = 2.0\%$	$7.5 \cdot 10^{-7}$	0.1133	0.2312	17

Table 1: Compression test of biological tissue with one hard lump, cf. figure 6: Performance and accuracy of the proposed variationally consistent adaptive finite element methods (For the *Standard* method, a 20x20 uniform discretization has been used.)

of the numerical solution. Furthermore, the influence of the data noise on the predicted stiffness distribution is again obvious. It bears emphasis that the not monotonically decreasing shear modulus error in figure 12 does not contradict the variational consistency of the algorithm, since consistency does only apply to the shear modulus error (the function to be minimized is based on the displacement error).

For comparing the performance of both variationally consistent adaptive finite element methods, their induced errors, together with their computing times, are summarized in table 1. The results corresponding to a uniformly refined mesh are also included in that table. Within the comparison, the number of mesh refinement steps has been chosen such that the adaptive schemes show, at least, the same accuracy as the standard approach. Therefore, only the computing times are important in what follows. As can be seen from table 1, with only one exception, the adaptive schemes are significantly more efficient than the conventional approach and thus, they require less computing time. This effect would be even more pronounced on multi processor computers, since the proposed adaptive

scheme can efficiently be implemented in parallel with a linear scalability. By comparing the results obtained from both adaptive schemes to one another, the rh -adaption seems to be more efficient. Accordingly, an effective algorithm should detect the material interfaces first yielding a qualitatively good result. Subsequently, the accuracy should be improved by enriching the underlying finite element space.

Remark 6.1 *According to the results discussed in the present subsection, data noise affects the results of the proposed algorithm. This is not very surprising, since the algorithm cannot distinguish between displacement fluctuations caused by material inclusions and those related to noise. Fortunately and as already mentioned in [2], an effective filter reducing the data noise can be developed. Although such a filter is beyond the scope of the present paper, the underlying idea will be briefly sketched. The displacement fluctuations associated with data noise induce a certain oscillation in the predicted shear modulus distribution. However, the respective wave length of this oscillation is several orders of magnitude smaller than the diameter of typical inclusions. Thus, if a predicted inclusion is smaller than a tolerance, it is an artifact. Based on this idea, filters can be designed.*

7 Conclusions

In the present paper, a novel finite element formulation suitable for computing efficiently the stiffness distribution in soft biological tissue has been presented. Starting from the numerical implementation of the inverse problem of finite strain hyperelasticity, the computing time was effectively reduced by using variationally consistent adaptive finite element methods. More precisely, a combined variational hr -refinement algorithm was advocated. While the h -adaption step as published in [2] enriches effectively the finite element space of admissible deformations and thus, it improves the solution quality of the forward problem, the novel variational r -adaption detects efficiently material interfaces such as those between healthy and diseased biological tissue. In sharp contrast to previous approaches, the nodal positions of the finite element triangulation were optimized within the r -adaption by considering the same minimization principle as that characterizing the inverse problem of hyperelasticity. Consequently, the proposed method is variationally consistent and it guarantees that the quality of the numerical solution is improved. Since quasi-incompressible biological tissue was considered, the r -adaption was combined with a mixed finite element formulation. Numerical analyses confirmed that the proposed hr -refinement algorithm is very promising for the inverse problem of finite strain hyperelasticity. Furthermore, it turned out that an r -refinement followed by an h -enrichment is more efficient than the other way around. Accordingly, an effective algorithm should detect the material interfaces first yielding a qualitatively good result and subsequently, the accuracy should be improved by enriching the underlying finite element space.

A Computation of $\mathbf{K}_e^{\Delta \mathbf{X}^{IJ}}$ – Sensitivities of the principle of virtual work with respect to the nodal coordinates \mathbf{X}^h

Here, the sensitivities of the principle of virtual work with respect to the nodal coordinates \mathbf{X}^I will be derived. For that purpose, (11)–(13) are considered and the pressure p as well

as the volume ratio Θ are re-written as functions depending on \mathbf{x}^h and \mathbf{X}^h (more precisely, they depend on the nodal variables \mathbf{x}^I and \mathbf{X}^I). Furthermore, a variation with respect to \mathbf{X}^I (or \mathbf{X}^h) will also result in a change in \mathbf{x}^I (or \mathbf{x}^h). Therefore, a variation of the principle of virtual work (12) with respect to the reference configuration \mathbf{X}^h reads

$$\mathbf{D}_x (\mathbf{D}_x \Pi^{\text{HW}} \cdot \boldsymbol{\eta}_x) \cdot \Delta \mathbf{X}^h \mathbf{x} + \mathbf{D}_X (\mathbf{D}_x \Pi^{\text{HW}} \cdot \boldsymbol{\eta}_x) \cdot \Delta \mathbf{X}^h = 0 \quad (42)$$

or equivalently in matrix notation

$$\boldsymbol{\eta}_x^I \cdot \mathbf{K}_e^{\Delta \mathbf{x}^{IJ}} \cdot \Delta \mathbf{X}^J \mathbf{x} + \boldsymbol{\eta}_x^I \cdot \mathbf{K}_e^{\Delta \mathbf{X}^{IJ}} \cdot \Delta \mathbf{X}^J = 0. \quad (43)$$

Here, only the contribution of one element has been considered and $\mathbf{K}_e^{\Delta \mathbf{x}^{IJ}}$ denotes the standard stiffness matrix of the underlying mixed finite element formulation, cf. [2]. According to

$$\begin{aligned} \Delta \mathbf{X} \mathbf{D}_x \Pi^{\text{HW}} &= \int_{\mathcal{B}} (\mathbf{D}_X (\text{Grad } \boldsymbol{\eta}_x) \cdot \Delta \mathbf{X}^h) : \mathbf{P} \, dV \\ &+ \int_{\mathcal{B}} \text{Grad } \boldsymbol{\eta}_x : (\mathbf{D}_X (\mathbf{P}) \cdot \Delta \mathbf{X}^h) \, dV \\ &+ \int_{\mathcal{B}_\xi} (\text{Grad } \boldsymbol{\eta}_x : \mathbf{P}) (\mathbf{D}_X (\det \mathbf{F}_{\hat{\Phi}}) \cdot \Delta \mathbf{X}^h) \, dV_\xi, \end{aligned} \quad (44)$$

the matrix $\mathbf{K}_e^{\Delta \mathbf{X}^{IJ}}$ representing the sensitivities of the residual forces with respect to the nodal coordinates \mathbf{X}^h (\mathbf{X}^I) can be decomposed into three terms, i.e.,

$$\boldsymbol{\eta}_x^I \cdot \mathbf{K}_e^{\Delta \mathbf{X}^{IJ}} \cdot \Delta \mathbf{X}^J = \boldsymbol{\eta}_x^I \cdot \left(\mathbf{K}_{1e}^{\Delta \mathbf{X}^{IJ}} + \mathbf{K}_{2e}^{\Delta \mathbf{X}^{IJ}} + \mathbf{K}_{3e}^{\Delta \mathbf{X}^{IJ}} \right) \cdot \Delta \mathbf{X}^J. \quad (45)$$

By further extending the first term

$$\begin{aligned} &\int_{\mathcal{B}} (\mathbf{D}_X (\text{Grad } \boldsymbol{\eta}_x) \cdot \Delta \mathbf{X}^h) : \mathbf{P} \, dV = \\ &\int_{\mathcal{B}} \left(\frac{\partial \boldsymbol{\eta}_x}{\partial \boldsymbol{\xi}} \cdot \left(\frac{\partial \mathbf{F}_{\hat{\Phi}}^{-1}}{\partial \mathbf{F}_{\hat{\Phi}}} : \frac{\partial \Delta \mathbf{X}^h}{\partial \boldsymbol{\xi}} \right) \right) : \mathbf{P} \, dV \end{aligned} \quad (46)$$

as well as the third term

$$\begin{aligned} &\int_{\mathcal{B}_\xi} (\text{Grad } \boldsymbol{\eta}_x : \mathbf{P}) \mathbf{D}_X (\det \mathbf{F}_{\hat{\Phi}}) \cdot \Delta \mathbf{X}^h \, dV_\xi = \\ &\int_{\mathcal{B}} \left(\left(\frac{\partial \boldsymbol{\eta}_x}{\partial \boldsymbol{\xi}} \cdot \mathbf{F}_{\hat{\Phi}}^{-1} \right) : \mathbf{P} \right) \mathbf{F}_{\hat{\Phi}}^{-T} \cdot \frac{\partial \Delta \mathbf{X}^h}{\partial \boldsymbol{\xi}} \, dV \end{aligned} \quad (47)$$

in Eq. (44), the matrices $\mathbf{K}_{1e}^{\Delta \mathbf{X}^{IJ}}$ and $\mathbf{K}_{3e}^{\Delta \mathbf{X}^{IJ}}$ are computed as

$$K_{1e}^{\Delta \mathbf{X}^{IJ}} = \int_{\mathcal{B}_0^e} -\frac{\partial N_I^\varphi}{\partial \xi_l} F_{\hat{\Phi}lj}^{-1} F_{\hat{\Phi}mk}^{-1} P_{ik} \frac{\partial N_J^\varphi}{\partial \xi_m} \, dV_e \quad (48)$$

$$K_{3e}^{\Delta \mathbf{X}^{IJ}} = \int_{\mathcal{B}_0^e} \frac{\partial N_I^\varphi}{\partial \xi_l} F_{\hat{\Phi}lk}^{-1} P_{ik} F_{\hat{\Phi}mj}^{-1} \frac{\partial N_J^\varphi}{\partial \xi_m} \, dV_e. \quad (49)$$

The only stiffness matrix that remains to be computed is related to the second term in Eq. (44). For its derivation, the linearization of the first Piola-Kirchhoff stress tensor $\mathbf{P}(\boldsymbol{\varphi}, p, \Theta)$ for fixed spatial coordinates \boldsymbol{x}^h resulting in

$$\begin{aligned} \int_{\mathcal{B}} \text{Grad } \boldsymbol{\eta}_{\boldsymbol{x}} : (\mathbf{D}_{\mathbf{X}}(\mathbf{P}(\boldsymbol{\varphi}, p, \Theta)) \cdot \Delta \mathbf{X}^h) \, dV = \\ \int_{\mathcal{B}} \text{Grad } \boldsymbol{\eta}_{\boldsymbol{x}} : \left(\mathbf{D}_{\mathbf{X}} \mathbf{P} \cdot \Delta \mathbf{X}^h + \mathbf{D}_p \mathbf{P} \cdot \Delta \mathbf{X}^h p + \mathbf{D}_{\Theta} \mathbf{P} \cdot \Delta \mathbf{X}^h \Theta \right) \, dV. \end{aligned} \quad (50)$$

represents the starting point. Having in mind that $\mathbf{P} \neq \mathbf{P}(\Theta)$, Eq. (50) can formally be re-written as

$$\begin{aligned} \boldsymbol{\eta}_{\boldsymbol{x}}^I \cdot \mathbf{K}_{2e}^{\Delta \mathbf{X}^{IJ}} \cdot \Delta \mathbf{X}^J = \\ \boldsymbol{\eta}_{\boldsymbol{x}}^I \cdot \left(\mathbf{K}_{\Delta \mathbf{X}^e}^{\Delta \mathbf{X}^{IJ}} \cdot \Delta \mathbf{X}^J + \mathbf{K}_{\Delta \mathbf{x}_{pe}}^{\Delta \mathbf{X}^{IJ}} \cdot \Delta \mathbf{X}^J p \right). \end{aligned} \quad (51)$$

By using the constitutive equations (6) and (7), together with the notation $\mathbb{A} = \partial \mathbf{P} / \partial \mathbf{F}$, the matrices $\mathbf{K}_{\Delta \mathbf{X}^e}^{\Delta \mathbf{X}^{IJ}}$ and $\mathbf{K}_{\Delta \mathbf{x}_{pe}}^{\Delta \mathbf{X}^{IJ}}$ in Eq. (51) are obtained as

$$K_{\Delta \mathbf{X}^e ij}^{\Delta \mathbf{X}^{IJ}} = \int_{\mathcal{B}_0^e} -\frac{\partial N_I^\varphi}{\partial \xi_l} F_{\hat{\boldsymbol{\Phi}} lk}^{-1} \mathbb{A}_{ikmn} F_{mj} F_{\hat{\boldsymbol{\Phi}} on}^{-1} \frac{\partial N_J^\varphi}{\partial \xi_o} \, dV_e \quad \text{and} \quad (52)$$

$$K_{\Delta \mathbf{x}_{pe} ij}^{\Delta \mathbf{X}^{IJ}} = \int_{\mathcal{B}_0^e} \frac{\partial N_I^\varphi}{\partial \xi_l} F_{\hat{\boldsymbol{\Phi}} lk}^{-1} J F_{ki}^{-1} N_J^p \, dV_e. \quad (53)$$

Finally, the sensitivity $\Delta \mathbf{X}^J p$ is derived by linearizing the weak forms (11) and (12) for fixed \boldsymbol{x}^h . A lengthy, but nevertheless straightforward, computation yields

$$\begin{aligned} \Delta \mathbf{X}^J p = \frac{1}{V_e} \int_{\mathcal{B}} \frac{\partial^2 U(\Theta)}{\partial \Theta^2} \, dV \Delta \mathbf{X}^J \Theta \\ + \left(\int_{\mathcal{B}} \left(\frac{\partial U(\Theta)}{\partial \Theta} - p \right) \mathbf{F}_{\hat{\boldsymbol{\Phi}}}^{-T} \cdot \frac{\partial N_J^\varphi}{\partial \boldsymbol{\xi}} \, dV \right) \cdot \Delta \mathbf{X}^J \end{aligned} \quad (54)$$

and

$$\Delta \mathbf{X}^J \Theta = \frac{1}{V_e} \left(\mathbf{M}_{\Delta \mathbf{X}^1}^{\Delta \mathbf{x} \Theta^J} + \mathbf{M}_{\Delta \mathbf{X}^2}^{\Delta \mathbf{x} \Theta^J} \right) \cdot \Delta \mathbf{X}^J \quad (55)$$

with

$$M_{1 \Delta \mathbf{X}^j}^{\Delta \mathbf{x} \Theta^J} = \int_{\mathcal{B}} -J F_{lk}^{-1} F_{kj} F_{\hat{\boldsymbol{\Phi}} ml}^{-1} \frac{\partial N_J^\varphi}{\partial \xi_m} \, dV \quad \text{and} \quad (56)$$

$$M_{2 \Delta \mathbf{X}^j}^{\Delta \mathbf{x} \Theta^J} = \int_{\mathcal{B}} (J - \Theta) F_{\hat{\boldsymbol{\Phi}} kj}^{-1} \frac{\partial N_J^\varphi}{\partial \xi_k} \, dV. \quad (57)$$

By combining Eqs. (51)–(57), the stiffness matrix $\mathbf{K}_{2e}^{\Delta \mathbf{X}^{IJ}}$ can be computed.

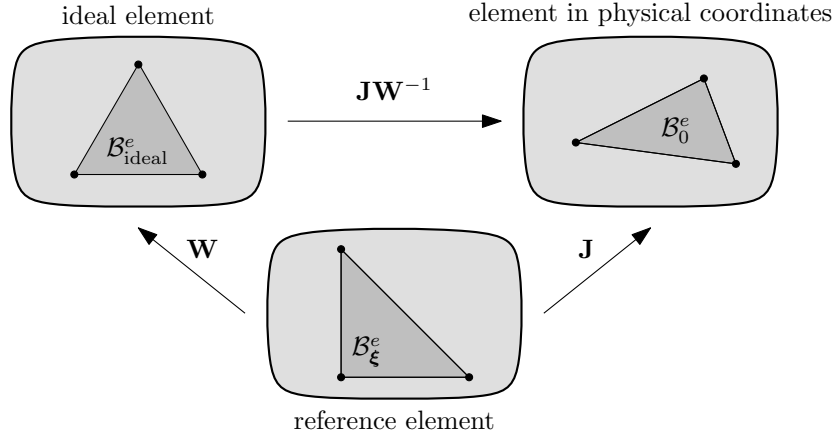


Figure 13: Different configurations of a simplex element

B A triangle shape measure

In this appendix, the simplex shape measure as advocated in [12, 19, 20], together with its linearization, is summarized. This shape measure is based on the condition number of the mapping connecting an element e to its ideal counterpart (all edges have the same length). Clearly, this mapping measures the deviation of the physical to the ideal simplex. According to Fig. 13, it is given by $\mathbf{B} \in \mathcal{L}(\mathbb{R}^2, \mathbb{R}^2)$ with $\mathbf{B} : \boldsymbol{\xi} \mapsto \mathbf{J} \cdot \mathbf{W}^{-1} \cdot \boldsymbol{\xi}$. In what follows and without loss of generality, the reference element

$$\Omega_M = \text{span}\{\mathbf{0}; \mathbf{e}_1; \mathbf{e}_2\} \quad (58)$$

and its ideal counterpart

$$\Omega_{\text{ideal}} = \text{span}\{\mathbf{0}; \mathbf{e}_1; (1/2, \sqrt{3}/2)\} \quad (59)$$

are considered. Consequently, the mapping connecting Ω_M to Ω_{ideal} is characterized by the matrix

$$\mathbf{W} = \begin{pmatrix} 1 & 0.5 \\ 0 & \sqrt{3}/2 \end{pmatrix}, \quad (60)$$

where \mathbf{J} is the classical JACOBIAN matrix. It can be shown that

$$g(\mathbf{J}) = \kappa_{\min}/\kappa(\mathbf{J} \cdot \mathbf{W}^{-1}) \quad (61)$$

is a shape measure for simplex elements with κ being the condition number of the respective element and κ_{\min} denoting the condition number of an ideal element. Furthermore, g fulfills the following criteria defining a mathematically sound simplex shape measure, cf. [6]:

- g is continuous
- $g = 0 \iff e$ is degenerated
- $g = 1 \iff e$ is ideal (all edges have the same length)
- g is invariant with respect to translations, rotations and the size of the considered element.

Consequently, the shape of two simplex elements can be compared to one another simply by evaluating the function g , i. e.,

$$g(\mathbf{J}^{(1)}) > g(\mathbf{J}^{(2)}) \iff \text{the shape of element 1 is better.} \quad (62)$$

Evidently, this maximum principle is equivalent to

$$\kappa(\mathbf{J}^{(1)} \mathbf{W}^{-1}) < \kappa(\mathbf{J}^{(2)} \mathbf{W}^{-1}) \iff \text{the shape of element 1 is better.} \quad (63)$$

It is noteworthy that criterion (63) is equivalent to minimizing the interpolation error, cf. [24].

Based on criterion (63) a given initial triangulation can be improved (with respect to the aspect ratios and thus, the interpolation error) by applying the optimization strategy

$$\inf_{\mathbf{X}^h} \mathfrak{h}_{\text{geo}} \quad \text{with} \quad \mathfrak{h}_{\text{geo}} = \sum_{i=1}^{n_{\text{ele}}} (f(\mathbf{J}_i))^p \quad \text{and} \quad f(\mathbf{J}) = \kappa(\mathbf{J} \cdot \mathbf{W}^{-1}). \quad (64)$$

In what follows, the condition number based on the FROBENIUS norm is used, i. e., $f(\mathbf{A}) = (\mathbf{A} : \mathbf{A}) (\mathbf{A}^{-1} : \mathbf{A}^{-1})$ with $\mathbf{A} := \mathbf{J} \cdot \mathbf{W}^{-1}$. The linearization of \mathfrak{h} (more precisely, that of f) necessary for a gradient-type optimization such as the L-BFGS-B algorithm can be computed in a straightforward manner. Combining

$$\frac{\partial f}{\partial X_z} = \frac{\partial f}{\partial A_{oj}} W_{jp}^{-T} \frac{\partial J_{op}}{\partial X_z}. \quad (65)$$

with

$$\mathbf{J} = \begin{bmatrix} X_1^{(2)} - X_1^{(1)} & X_1^{(3)} - X_1^{(1)} \\ X_2^{(2)} - X_2^{(1)} & X_2^{(3)} - X_2^{(1)} \end{bmatrix}, \quad (66)$$

results finally in

$$\frac{\partial f}{\partial \mathbf{X}^{(i)}} = \frac{\partial f}{\partial \mathbf{A}} \cdot \mathbf{W}^{-T} \cdot \mathbf{n}^{(i)}, \quad (67)$$

with

$$\mathbf{n}^{(1)} = (-1; -1) \quad \mathbf{n}^{(2)} = (1; 0) \quad \mathbf{n}^{(3)} = (0; 1). \quad (68)$$

The second derivatives of f necessary for a Newton-type iteration can be found in [24].

References

- [1] Ainsworth M and Oden J T 2000 *A Posteriori Error Estimation in Finite Element Analysis* Wiley.
- [2] Arnold A, Reichling S, Bruhns O T and Mosler J 2010 *Physics in Medicine and Biology* **55**.
- [3] Braun M 1997 *Proc. Estonian Acad. Sci. Phys. Math.* **46**, 24–31.
- [4] Byrd R H, Lu P, Nocedal J and Zhu C 1994 *SIAM Journal on Scientific Computing* **16**, 1190–208.
- [5] Ciarlet P 1988 *Mathematical elasticity, volume I: Three-dimensional elasticity* Springer Netherlands.

-
- [6] Dompierre J, Labbe P, Guibault F and Camarero R 1998 *Proceedings, 7th International Meshing Roundtable* pp. 459–78.
- [7] Doyley M M, Meaney P M and Bamber J C 2000 *Physics in Medicine and Biology* **45**(6), 1521–40.
- [8] Engl H, Hanke M and Neubauer A 2003 *Regularization of Inverse Problems* Kluwer Academic Publishers.
- [9] Eshelby J D 1951 *Philos. Trans. Roy. Soc. London A* **244**, 87–112.
- [10] Eshelby J D 1975 *J. Elasticity* **5**, 321–335.
- [11] Felippa C A 1976 *Applied Mathematical Modelling* **1**, 239–44.
- [12] Freitag L and Knupp P N 2002 *International Journal for Numerical Methods in Engineering* **53**, 1377–91.
- [13] Fung Y C 1993 *Biomechanics: Mechanical Properties of Living Tissues* Springer.
- [14] Garra B S, Cespedes E I, Ophir J, Spratt S R, Zuurbier R A, Magnant C M and Pennanen M F 1997 *Radiology* **202**, 79–86.
- [15] Gokhale N H, Barbone P E and Oberai A A 2008 *Inverse Problems* **24**, 26pp.
- [16] Hughes T J R 2000 *The Finite Element Method* Dover Publications.
- [17] Kallel F and Bertrand M 1996 *IEEE Transactions on Medical Imaging* **15**(3), 299–313.
- [18] Khaled W A M 2007 Displacement estimation analyses for reconstructive ultrasound elastography using finite-amplitude deformations PhD thesis Ruhr-Universität Bochum.
- [19] Knupp P 2000a *International Journal for Numerical Methods in Engineering* **48**, 401–20.
- [20] Knupp P 2000b *International Journal for Numerical Methods in Engineering* **48**, 1165–85.
- [21] Kuhl E, Askes H and Steinmann P 2004 *Computer Methods in Applied Mechanics and Engineering* **193**(39-41), 4207–22.
- [22] Marsden J E and Hughes T J R 1994 *Mathematical Foundations of Elasticity* Dover Publications.
- [23] McNeice, G. M. ; Marcal P V 1973 *Trans. ASME, J. of Eng. for Industry* **95**, 186–90.
- [24] Mosler J 2007 *On the numerical modeling of localized material failure at finite strains by means of variational mesh adaption and cohesive elements* Habilitation, Ruhr University Bochum, Germany.
- [25] Mosler J and Ortiz M 2006 *International Journal for Numerical Methods in Engineering* **67**, 1272–89.

- [26] Mosler J and Ortiz M 2007 *International Journal for Numerical Methods in Engineering* **72**, 505–523.
- [27] Mosler J and Ortiz M 2009 *International Journal for Numerical Methods in Engineering* **77**, 437–450.
- [28] Oberai A A, Gokhale N H, Doyley M M and Bamber J C 2004 *Physics in Medicine and Biology* **49**, 2955–74.
- [29] Oberai A A, Gokhale N H and Feijo G R 2003 *Inverse Problems* **19(2)**, 297–313.
- [30] O’Donnell M, Skovoroda A R, Shapo B M and Emelianov S 1994 *IEEE transactions on ultrasonics, ferroelectrics, and frequency control* **41**, 314–25.
- [31] Ophir J, Céspedes I, Ponnekanti H, Yazdi Y and Li X 1991 *Ultrasonic Imaging* **13**, 111–34.
- [32] Pellot-Barakat C, Frouin F, Insana M and Herment A 2004 *IEEE Transactions on Medical Imaging* **23**, 153–63.
- [33] Reichling S 2007 Das inverse Problem der quantitativen Ultraschallelastografie unter Berücksichtigung großer Deformationen PhD thesis Ruhr-Universität Bochum.
- [34] Rivara M C 1991 *Journal of Computational and Applied Mathematics* **36**, 79–89.
- [35] Rivara M C 1997 *International Journal for Numerical Methods in Engineering* **40**, 3313–24.
- [36] Schenk O and Gärtner K 2004 *Journal of Future Generation Computer Systems* **20**, 475–87.
- [37] Schenk O and Gärtner K 2006 *Electronic Transactions on Numerical Analysis* **23**, 158–79.
- [38] Simo J C and Hughes T J R 1998 *Computational Inelasticity* Vol. 7 of *Interdisciplinary Applied Mathematics* Springer-Verlag New York.
- [39] Simo J C and Taylor R L 1991 *Computer Methods in Applied Mechanics and Engineering* **85**, 273–310.
- [40] Simo J C, Taylor R L and Pister K S 1985 *Computer Methods in Applied Mechanics and Engineering* **51**, 177–208.
- [41] Skovoroda A R, Emelianov S Y and O’Donnell M 1995 *IEEE Transactions on Ultrasonics, Ferroelectrics and Frequency Control* **42(4)**, 747–65.
- [42] Sumi C, Suzuki A and Nakayama K 1995 *IEEE Transactions on Biomedical Engineering* **42(2)**, 193–202.
- [43] Thoutireddy P and Ortiz M 2004 *International Journal for Numerical Methods in Engineering* **61**, 1–21.
- [44] Truesdell C and Noll W 2004 *The Non-Linear Field Theories of Mechanics* 3rd edn Springer-Verlag.

- [45] Verfürth R 1996 *A Review of A Posteriori Error Estimation and Adaptive Mesh-Refinement Techniques* Wiley-Teubner.
- [46] Washizu K 1982 *Variational Methods in Elasticity and Plasticity* 3 edn Pergamon Press.
- [47] Zhu C, Byrd R H, Lu P and Nocedal J 1997 *ACM Transactions on Mathematical Software* **23**, 550–60.
- [48] Zienkiewicz O C and Taylor R L 2000 *The Finite Element Method* Vol. 1 5 edn Butterworth-Heinemann.